
Spectral and Timing analysis of the HMXB GX 304–1 with *Suzaku*

Bachelorarbeit aus der Physik

vorgelegt von

Ralf Ballhausen

Bamberg, 2. September 2013



Dr. Karl Remeis-Sternwarte Bamberg
Astronomisches Institut der
Friedrich-Alexander-Universität Erlangen-Nürnberg



ERLANGEN CENTRE
FOR ASTROPARTICLE
PHYSICS

Betreuer: Prof. Dr. Jörn Wilms

Contents

1. Introduction	4
2. GX 304–1 and Suzaku - a brief overview	5
2.1. GX 304–1	5
2.2. <i>Suzaku</i>	6
2.2.1. XIS	6
2.2.2. HXD	7
3. Data acquisition and reduction	8
4. Timing analysis and results	11
4.1. Pulse period determination with epoch folding	11
4.2. Pulse profiles	13
5. Spectroscopy	19
5.1. Phase averaged spectroscopy	20
5.1.1. Partial coverer	20
5.1.2. Cut-off powerlaw with blackbody	21
5.1.3. NPEX continuum model	22
5.2. Phase resolved spectroscopy	25
5.2.1. Extraction of phase resolved spectra	25
5.2.2. Partial coverer and blackbody model	25
6. Conclusions	32
A. Best fit parameters of phase resolved spectra with partial coverer	35
B. Best fit parameters of phase resolved spectra with blackbody model	39

Abstract

This Bachelor thesis describes the methods and results of spectral and timing analysis of a *Suzaku* observation of GX 304–1 of an outburst in 2012 January. The pulse period was determined by epoch folding and found to be 274.88 s, agreeing with earlier observations. The pulse profiles show a strong dependence on energy, becoming apparent in a complex three peak structure in the low energy band which evolves to a two peak structure with increasing energy. One peak is vanishing at ~ 18 keV. Phaselags were also detected for this source but the individual peaks do not shift uniformly. The phase averaged spectra can be well described with a partial coverer model as well as a high energy cut-off powerlaw with an additional blackbody component as continuum model, but not with a NPEX model. Both models require a cyclotron resonant scattering feature around ~ 54 keV and fluorescence iron line. Pulse phase resolved spectra have been extracted for eight equally spaced phase intervals. However, the empirical models fail to provide a satisfying description of all pulse phase resolved spectra. This emphasizes again the importance of the development of physical continuum models.

1. Introduction

Compared to other branches of astronomy, X-ray astronomy is rather young. As the earth's atmosphere is opaque for X-rays, observations in that energy range were beyond the means until technical possibilities to reach space or at least the outer layers of the atmosphere became available. In 1949, Herbert Friedman et al. used a V-2 rocket carrying Geiger counters to explore the sun's extreme ultraviolet and soft X-ray radiation. They detected significant X-ray flux from the solar corona above 87 km (for details see Friedman et al. 1951). These promising discoveries smoothed the way for rapid advances in X-ray astronomy. Thirteen years later, a team of scientists led by Riccardo Giacconi, originally searching for X-rays from the moon, provided evidence for X-ray sources outside the solar system. They were also using rocket-carried Geiger counters and successfully detected the first galactic X-ray source *Scorpius X-1* (Giacconi et al. 1962). In 1970 the first X-ray satellite *UHURU* was launched, providing much longer observation time and therefore the opportunity to search for X-ray sources systematically. However, these early type detectors only used collimators with rather low angular resolution to determine the direction of the sources. A revolutionary progress, not only on the spatial resolution but also on the effective area, was made by the development of Wolter telescopes, i.e., optical systems taking advantage of the effect of total reflection to collect and focus X-rays. This technique had already been proposed in 1952 (Wolter 1952), however, because of the very high demands on the accuracy of the mirrors, these were first technically feasible in the late 1970s. The first X-ray observatory making use of such a telescope was *HEAO-2* (also known as *Einstein Observatory*) in 1978 (Giacconi et al. 1979). Since then, numerous X-ray missions have been carried out, following the advancing technologies of photon detection and measurement. A large number of X-ray sources have thereby been detected and catalogued during extended sky surveys (see, e.g., Voges et al. 1999, for *ROSAT* all sky survey). Among these, neutron star binaries form a remarkable class of astrophysical objects. Mostly invisible in the optical, neutron stars tend to be bright in X-rays due to mass accretion from the companion star. Since neutron stars have the strongest magnetic fields known in the universe, the accretion and radiation processes are both challenging and instructive. Various physical phenomena and effects have to be taken into account, including e.g. quantum mechanics, plasma physics and magneto-hydrodynamics. Therefore, significant effort is made to get to a better understanding of these processes through theoretical modelling and simulations as well as empirical methods. GX 304–1 is a High Mass X-ray Binary (HXMB) with a neutron star that has been repeatedly observed with growing interest over the last years. During its 2012 January outburst, GX 304–1 was monitored with different X-ray observatories simultaneously, among these *INTEGRAL*, *Swift* and *Suzaku*. The analysis of the obtained data with *Suzaku* and its results will be presented in this thesis.

2. GX 304–1 and Suzaku - a brief overview

2.1. GX 304–1

GX 304–1 is a transient X-ray pulsar that was already discovered in the early era of X-ray astronomy during balloon experiments in 1967 October (see, e.g., Lewin et al. 1968). Observations carried out in the following years revealed pulsations and flaring indicating a neutron star binary. In 1977, McClintock et al. as well as Huckle et al. found the pulse period to be around 272 s using data from the SAS-3 satellite and *Ariel V*, respectively. The optical companion was identified with a Be star by Mason et al. (1978). The first estimate of the orbital period was presented by Priedhorsky & Terrell in 1983. They observed periodic flaring with a periodicity of 132.5 ± 0.4 d, which they ascribed to varying mass accretion rates in an eccentric orbit. It is assumed that the Be star emitting matter by strong stellar winds forms an equatorial disc around it and the neutron star’s passing through that disk close to the periastron results in an outburst. Although the source showed significant X-ray flux and flaring at the time of its discovery, it had been in an off state since 1980 where the X-ray flux was far below its former values, even during the predicted flares (Pietsch et al. 1986). In 2009, *MAXI/GSC* detected an outburst, indicating renewed activity of the source (Yamamoto et al. 2009). Since then, GX 304–1 has shown regular outbursts again with a periodicity similar to the estimated orbital period. Spectral analysis of *RXTE* and *Suzaku* data obtained during an outburst in 2010 August revealed the presence of a cyclotron scattering resonant feature (CSRF or *cyclotron line*) around 54 keV. The pulse profiles are strongly energy-dependent and also a change of the pulse period during the outburst was detected with the *RXTE* data (Yamamoto et al. 2011). Furthermore, these authors found the cyclotron line energy to vary and an indication of a positive correlation of the cyclotron line energy and luminosity, though at low confidence level. This correlation was later confirmed by Klochkov et al. in 2012. They made use of *INTEGRAL* observations covering the same outburst as presented in this thesis. The character of the correlation of cyclotron line energy and luminosity is of particular interest, as it gives inference of the accretion mechanism. It is a result of a displacement of the emitting region connected to luminosity. The positive correlation is theoretically predicted for sources in a subcritical accretion regime, i.e., the inflowing gas is decelerated by Coulomb breaking rather than by radiation pressure. In this case, the height of the emission region is expected to decrease with increasing luminosity which results in the observed correlation (Becker et al. 2012). Further analysis of this source was reported by Devasia et al. in 2011. The authors also used *RXTE* data covering most of the outburst in August 2010. They found the shape of the pulse profile to vary over the outburst. The detected pulse period of 275.37 s indicates, that the neutron star has spun down during its off state. The Power Density Spectra (PSD) show a Quasi Periodic Oscillation (QPO) with a fundamental frequency of $0.125 \pm$

0.002 Hz and the first harmonic. However, there are still many questions concerning this source. The orbital parameters are still not determined. Recent progresses in light-bending and CRSFs simulations promise deeper insights into the accretion geometry of this source. The complex structure of the pulse profiles is not completely understood and also the dependence of spectral parameters of flux and pulse phase has to be further investigated. These are only some reasons why astrophysicists of several different work groups are highly interested in GX 304–1 and that will certainly make it an important target to future observations and missions.

2.2. Suzaku

This section is supposed to summarize the most important characteristics, capabilities and limitations of the satellite used later in my analysis of data from GX 304–1. Unless otherwise noted, all technical specifications refer to *The Suzaku Technical Description*¹ provided by ISAS/JAXA and NASA/Goddard Space Flight Center. A more detailed description of the technical specifications of XIS and HXD are given by Koyama et al. (2007) and Takahashi et al. (2007), respectively.

The X-ray observatory *Suzaku* (or *Astro-E2*) is the recovery mission of *Astro-E* whose launch on 2000 February 10 failed because of a technical problem of the carrying M V rocket. *Suzaku* was then successfully launched on 2005 July 10. It was developed by the Institute of Space and Astronautical Science of Japan Aerospace Exploration Agency (ISAS/JAXA) in collaboration with NASA/GSFC and carries the X-ray Imaging Spectrometer (XIS), Hard X-ray Detector (HXD) and X-ray spectrometer (XRS). The XRS is a X-ray calorimeter with an intended energy resolution of 7 eV. Unfortunately, all the liquid helium necessary to achieve the performing temperature evaporated within three weeks. The XRS is therefore no longer functional. However, the loss of XRS did not affect the remaining two detectors XIS and HXD, which are still available for observations. One of the key features of *Suzaku* is its high sensitivity in wide-band observations, together with low background count rates and its high energy resolution below 1 keV (Mitsuda et al. 2007).

2.2.1. XIS

The XIS consists itself of four single CCD detectors placed in the focal plane of four individual Wolter Type-I telescopes. XIS1 is back-illuminated, the other ones are front-illuminated. Back-illuminated CCD sensors are more sensitive to soft X-rays, whereas front-illumination shows advantages in the hard X-ray response. With this configuration, the XIS covers an energy range from 0.2–12 keV with a $18' \times 18'$ field of view. Regrettably, XIS2 was hit by micro-meteorite impact in 2009 November and became unusable. As all semiconductor detectors are affected by high temperatures, the XIS is kept at -90°C with thermo-electric coolers. There are several clocking and editing modes available for the XIS. The clocking modes define different readout strategies of the CCD pixels. The *Normal mode* without any further options specifies a full readout with an effective exposure time per frame of 8 s. The window and burst option allows to restrict the readout in space and time, respectively. Both options can

¹ http://heasarc.gsfc.nasa.gov/docs/suzaku/prop_tools/suzaku_td/

be combined. The other mode is called *P-sum mode* and is used for stacked readout. The editing modes specify different telemetry formats. In Normal clocking mode, the editing modes 2×2 , 3×3 and 5×5 are available, whereas the 2×2 mode only works for front illuminated sensors. These modes determine how many pixels around an event are registered. If, for example, an event is registered in a certain pixel (center) in 3×3 mode, the pulse height values of the center pixel, together with the 8 pixels around it, are telemetered to ground. P-sum mode has only one editing mode called *timing*.

2.2.2. HXD

The HXD is a non-imaging detector sensitive for the hard X-ray band between 10 keV and 600 keV. It is a combination of the two detectors PIN and GSO. PIN is an array of silicon diodes placed behind a collimator. Each diode is 2 mm thick and has an effective area of 16.5×16.5 mm². Above ~ 70 keV, the diodes become increasingly transparent for X-rays. For this reason, GSO is located behind the PIN diode array. GSO is a phoswich scintillation detector, built of Gadolinium Silicate ($\text{Gd}_2\text{SiO}_5(\text{Ce})$) crystals and both detectors are actively shielded by Bismuth Germanate ($\text{Bi}_4\text{Ge}_3\text{O}_{12}$). These two scintillators have very different rise/decay times, offering the possibility to distinguish between X-ray signals and background events with one photomultiplier tube. The collimator defines a field of view of $34' \times 34'$ FWHM below 100 keV. This is rather narrow, compared for example to the field of view of *RXTE*-HXTE of 1° FWHM (Rothschild et al. 1998), and advantageous to reduce background. Above 100 keV, however, the field of view of HXD widens up to 4.5° as the collimator becomes more and more transparent towards higher energies. The background of HXD is estimated without off-source observations. To model the non X-ray background, an empirical model is fitted to data collected during Earth occultation. Then the expected count rate can be calculated for any given time and a background event file is created using Monte Carlo simulations. Important parameters are, e.g., the geomagnetic cut-off rigidity and the time since passing the South Atlantic Anomaly, since these affect the activation of the detector material (Fukazawa et al. 2009).

3. Data acquisition and reduction

GX 304–1 was monitored by *Suzaku* during an outburst from 2012 January 31 to 2012 February 2. The midtime of the observation was MJD 55958.3 and the effective exposure time was ~ 16.5 ks. Figure 3.1 shows the observed section of the outburst as seen in the *Swift*/BAT lightcurve. The intensity was decreasing again around five days after the maximum. The obtained data were reprocessed with our standard *Suzaku* reprocessing routine, which basically runs `aepipeline` of HEASoft v6.13 to apply the latest calibration files to the raw data. The attitude of the satellite is not known precisely and mainly distorted by “thermal wobbling”. Therefore, a ftool called `aeattcor2` exists to create correct attitude files for *Suzaku* data to use for further analysis. The tool is based on the S-Lang script `aeattcor.sl`, originally written by John E. Davis. A small region around the source is marked and the script calculates the mean position of events with respect to time. For this, the a time grid is created and the mean X and Y position of the events occurring in each time bin is calculated. These positions will dither around their time averaged value because of the thermal wobbling. The time-depending offset of the instantaneous position from the mean value is then used to interpolate the new attitude file (see Uchiyama et al. 2008, for more details). In Figure 3.2, the mean X and Y position of the source is calculated for every 100 s and plotted against time. The variation, especially of the Y position shows the necessity of attitude correction. It is advisable to always check for attitude correction, since the effects of thermal wobbling are not always clearly obvious on the CCD chip image. Another effect that has to be considered is *pile-up*. Pile-up occurs when more than one photon hit an event detection-cell within one frame. The resulting event is then registered with approximately the summed energy of the single photons. Pile-up is nearly always an issue in imaging X-ray detectors and has to be considered as it biases the measured count rate and energy distribution. A real correction of pile-up is not possible, because a piled-up event can not be reconstructed and it is not always even known which events are single photon events and which are not. Therefore, an estimation of the pile-up is calculated in terms of a pile-up fraction, i.e., a probability for pile-up and regions with higher pile-up fraction than a certain threshold value are excluded from the source region. There are several empirical models to estimate pile-up where also simplifying assumptions are made. The one used for *Suzaku* data analysis expects the pile-up fraction to be $1 - \exp(-\Lambda)$, where Λ is the incident count rate, based on the assumption that piled and single photon events can be distinguished, e.g., due to grade migration (for details see Davis 2001, and *The Chandra ABC Guide to Pileup*²). In the case of *Suzaku*, attitude correction and pile-up estimation can of course only be done for XIS since HXD has no spatial resolution. Circular source and background region of each CCD chip were selected individually by hand (compare Figure 3.3). It should be noted that all XIS data were collected in burst mode. After these steps, lightcurves and spectra can easily be extracted with the *Suzaku* extraction scripts in Bamberg, which conveniently apply the tools `aeattcor2` and `pileest` to all

² http://cxc.harvard.edu/ciao/download/doc/pileup_abc.pdf

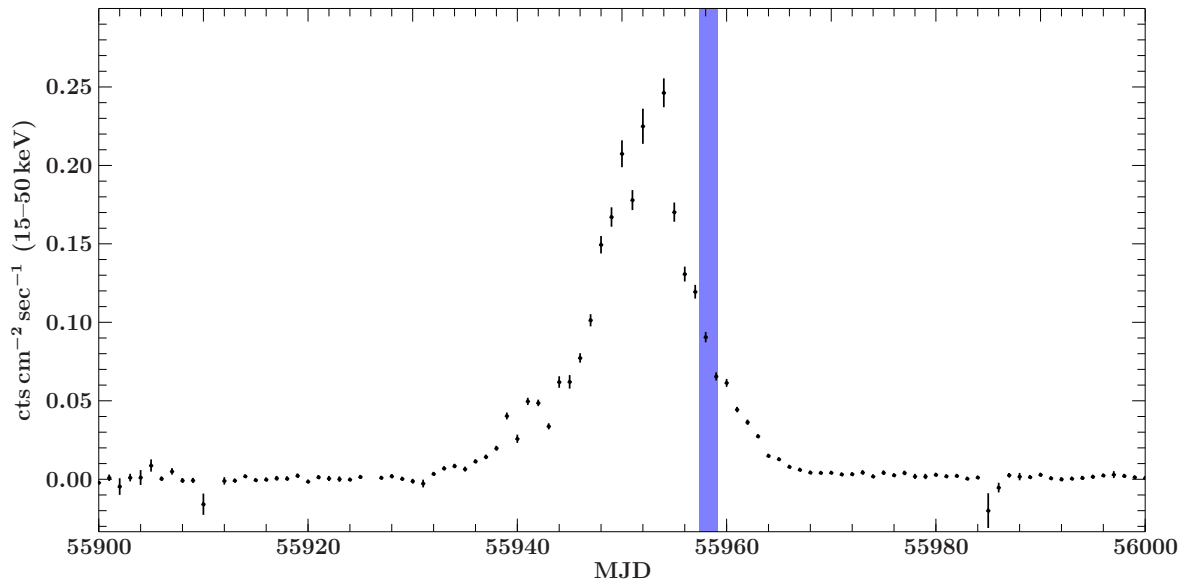


Fig. 3.1.: *Swift*/BAT lightcurve of the outburst in January 2012. The blue region marks the time of the *Suzaku* observation.

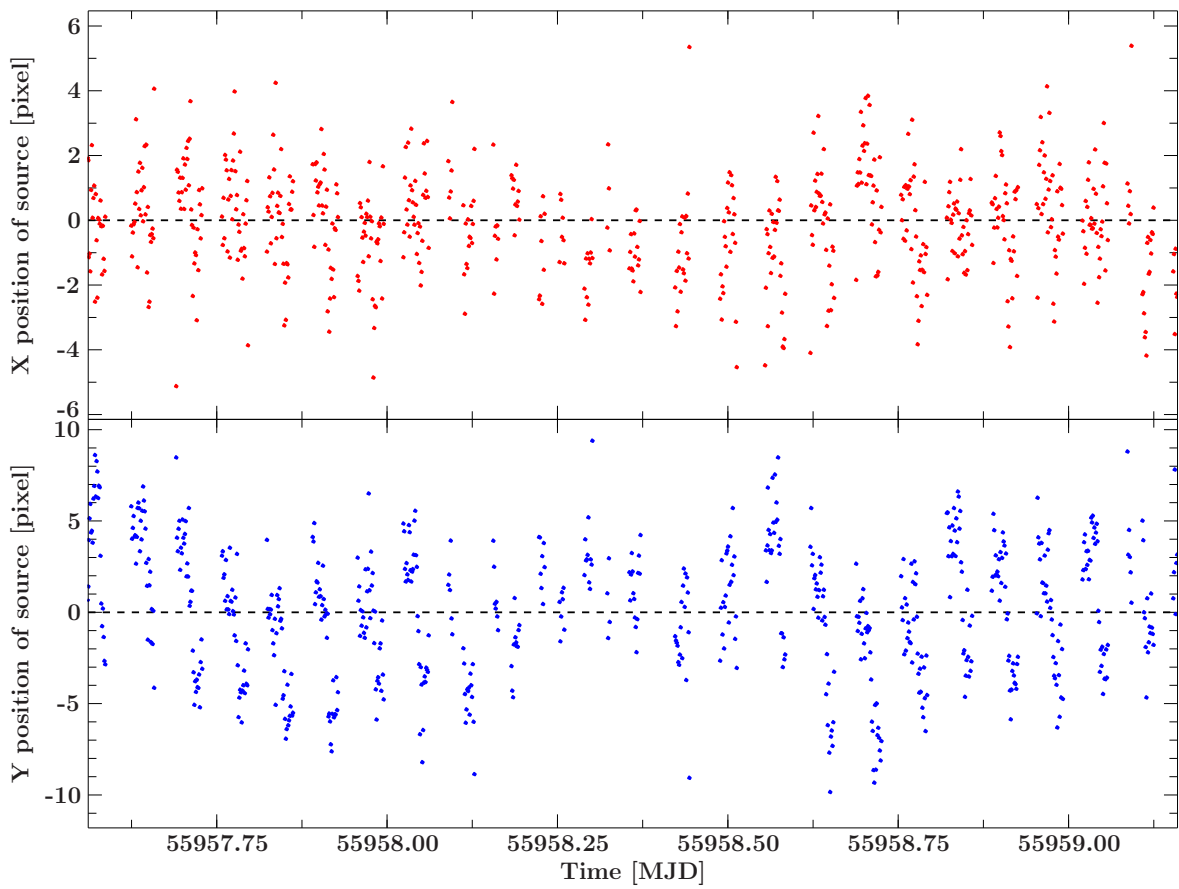


Fig. 3.2.: Variation of the X (red) and Y (blue) position of the source for XIS3. The dashed line indicates the overall mean position of the source.

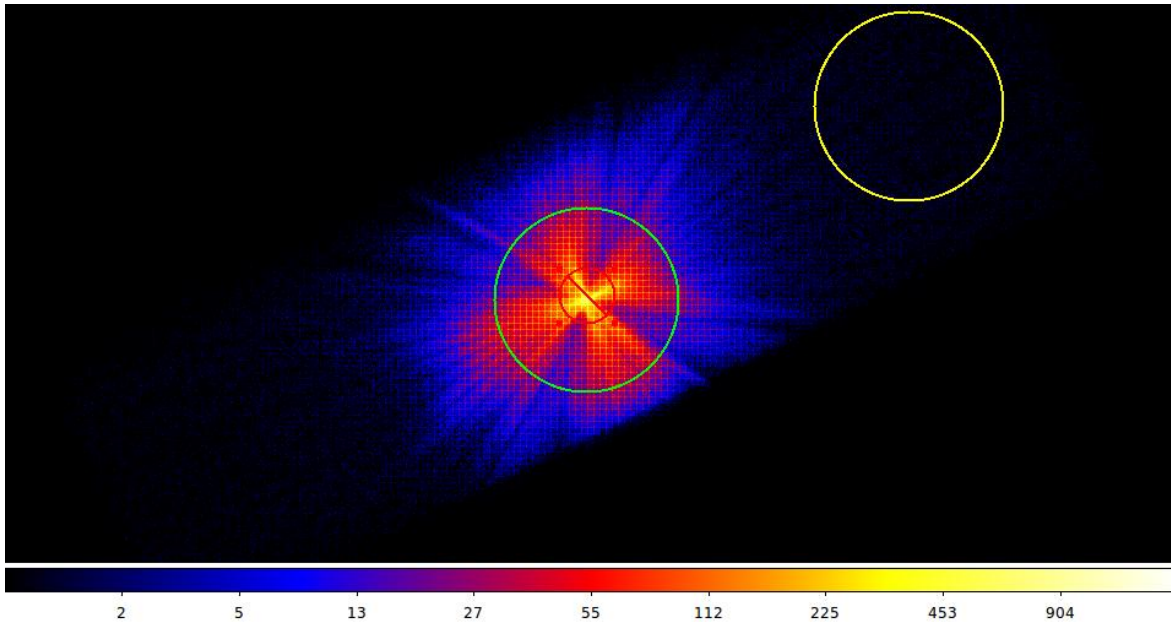


Fig. 3.3.: Sky image of XIS1 in 3×3 mode. The green circle indicates the selected source region, the yellow circle indicates the background region. The red circle indicates the region that was excluded due to pile-up.

of the XIS event files to create new attitude files and calculate the pile-up fraction. The central region around the neutron star showed significant pile-up. All regions with pile-up fraction larger than 4% were excluded from the source region. Finally, `xselect` is run automatically by the extraction scripts to extract lightcurves and spectra. All XIS detectors were run partly in 3×3 and 5×5 mode. The corresponding spectra were combined using `phaadd`, which also adds the background spectra and calculates a combined detector response matrix. All further spectral and timing analysis was performed with ISIS v1.6.2-24³. Another point worth mentioning for data reduction is barycentric correction. All event times of the reprocessed data are measured in the local system of reference of the satellite. As the satellite is in orbit around the Earth and the Earth itself is moving around the Sun, this system of reference differs from the barycentric system, i.e., the system of reference of an observer in the center of mass of the solar system, because of light travel times and Doppler shift. For timing analysis, it is crucial to convert all times to the barycentric system to get rid of these superposing effects. Therefore, barycentric correction was applied to all XIS and HXD event files by means of `aebarycen`, which is part of the `ftools`. The conversion between barycentric and local system of reference will again be important to extract pulse-phase resolved spectra and described in detail in section 5.2.1.

³ <http://space.mit.edu/cxc/isis/>

4. Timing analysis and results

It had already been mentioned in section 2.1 that GX 304–1 has early been discovered to be a X-ray pulsar. The name already indicates that these sources show periodically change in intensity, the so called pulsations. The pulse period is a fundamental parameter of X-ray pulsars but observation show, that it is not a constant, but changes over time due to transfer of angular momentum of the accreted matter. For GX 304–1 , the pulse period changed, e.g., between the time of its discovery and 2010 from ~ 272 s (McClintock et al. 1977; Huckle et al. 1977) to ~ 275 s (Devasia et al. 2011). One first step towards timing analysis is therefore to determine the pulse period, which is also an important input parameter for advanced analysis.

4.1. Pulse period determination with epoch folding

To determine the pulse period, one searches for periodicities in the lightcurve. A common method to search for periodicities in a given signal is to perform a *Fast Fourier Transform* (FFT) and then to look for peaks in the frequency domain or power spectral density (van der Klis 1989). Lightcurves from X-ray observations, however, normally contain a large number of gaps and the sections are of different length. This causes problems with FFT so this method is mostly not advantageous. Another, far easier way to find the pulse period is *epoch folding* (Leahy et al. 1983). The basic idea behind this method is the following: if one knows the pulse period and assumes that the pulse period does not change significantly during the time of the observation, one can split the lightcurve according to the pulse period and average over all the individual pieces with an additional binning. The resulting *pulse profile* should then show the count rate explicitly changing over time, reflecting the pulsation. If the assumed pulse period is not correct, then the pulses will be averaged over a long observation, and the pulse profile will appear less structured. This can now be used to search for the correct pulse period. An ISIS function called `epfold` exists that calculates the pulse profiles for a specified number of test periods in a period range and compares it to the mean count rate of the pulse profile. The returned χ^2 quantifies the “flatness” of the pulse profiles. Therefore, the χ^2 reaches its maximum value at the correct pulse period. The function can also be used with event data to avoid artificial features due to lightcurve binning and use the full time resolution of the event file. The pulse period of GX 304–1 is roughly known from previous observations. In Figure 4.1 the χ^2 value is plotted against the test periods. The binning of the pulse profiles was set to 32. All detectors agree nicely, although the peak of GSO is far less clear. The count rate in GSO is much lower than in the other detectors yielding a low signal-to-noise. For this reason GSO was not used for further pulse period determination. Although the pulse period determination with epoch folding is remarkably easy, proper error calculation with this method is difficult. One possible approach to error estimation, that was also applied here, is to use a Monte Carlo simulation. For this, the pulse profile is first calculated with the original pulse period. Then, a simulated lightcurve is created by interpolating the count rate

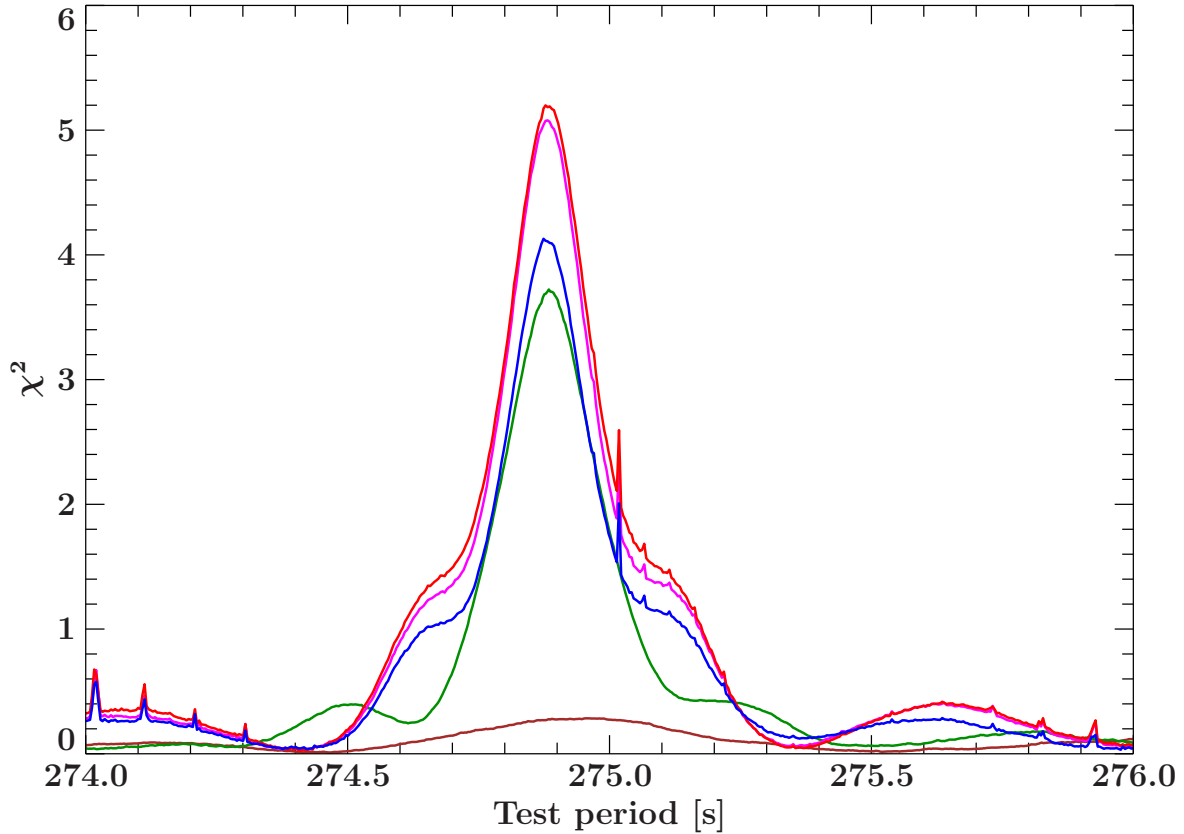


Fig. 4.1.: Results of epoch folding for all available detectors: XIS0 (blue), XIS1 (red), XIS3 (magenta), PIN (green) and GSO (brown).

Table 4.1.: Pulse periods obtained with the individual detectors and averaged value.

detector	pulse period [s]
XIS0	274.8737 ± 0.0021
XIS1	274.8778 ± 0.0034
XIS3	274.8818 ± 0.0031
PIN	274.8841 ± 0.0034
mean	274.8793 ± 0.0030

by means of the pulse profile. Gaussian noise is added to the simulated lightcurve. The simulated, noisy lightcurve is then again epoch folded. This process is repeated over and over again and the standard deviation of all the obtained pulse periods is taken as error for the original pulse period. However, it is questionable whether this really represents the uncertainty of the pulse period correctly. One important problem with this procedure is that time-dependent changes of the luminosity are not taken into account when simulating the lightcurve. Appending the averaged pulse profile to create a representative lightcurve is really a simplification. Furthermore, any change of the pulse period itself is ignored and the count rate distribution follows Poisson statistics. The estimated uncertainty is therefore probably too small. The individual values of the pulse periods of XIS and PIN are listed in Table 4.1. Their mean value of 274.8793 ± 0.0030 s is also used for all further analysis. The standard deviation of the individual pulse periods of XIS and PIN is 0.0046 s and is of the same order as estimated error.

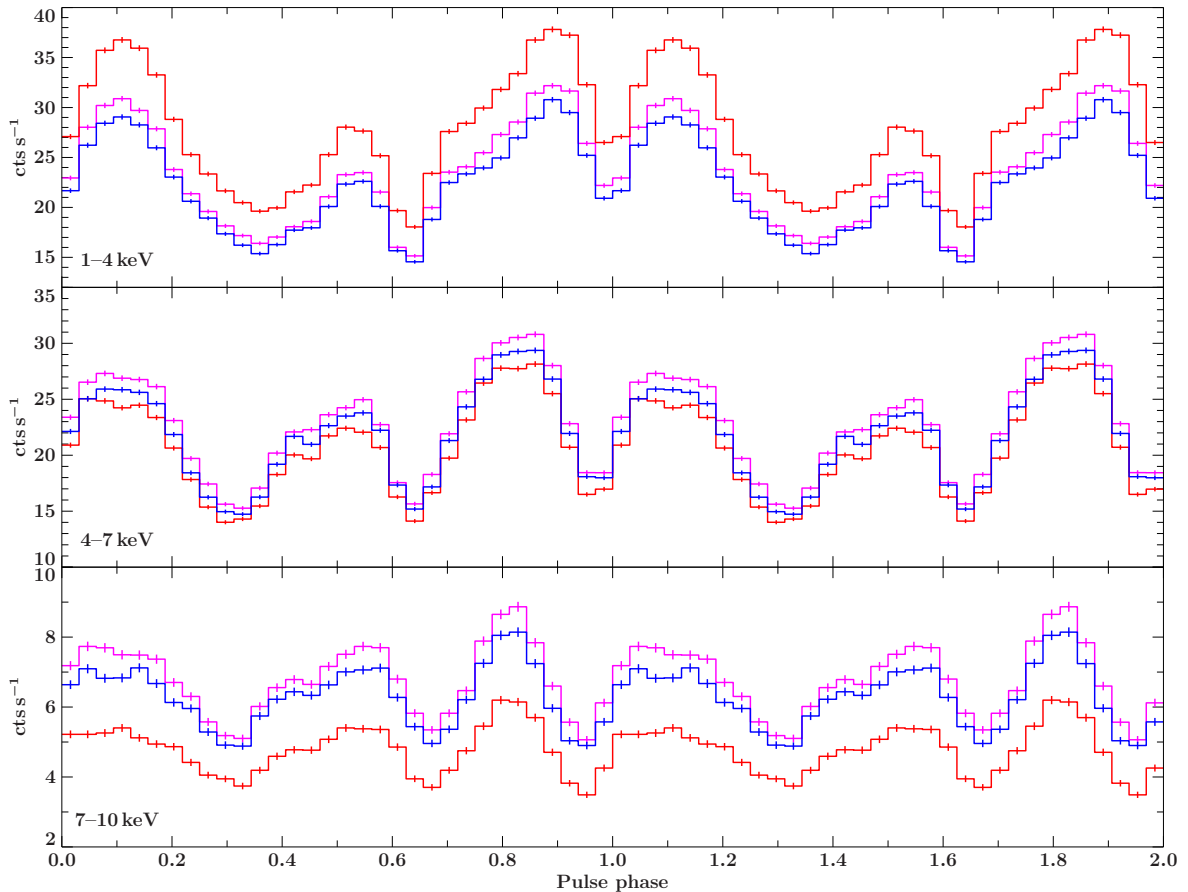


Fig. 4.2.: XIS pulse profiles for different energy bands. XIS0 (blue), XIS1 (red), XIS3 (magenta). Pulse profiles are shown twice for clarity.

4.2. Pulse profiles

As already described above in the process of epoch folding, a pulse profile can be calculated for a given pulse period. The pulse profile is simply the lightcurve folded modulo the pulse period and it shows the variation of the count rate over the pulse phase. As the neutron star is rotating, every pulse phase refers to a certain viewing angle under which the source is observed. From the accretion geometry of neutron star, one expects the X-ray emission mainly from the magnetic poles. The movement of the accreted matter inside the Alfvén radius is following the magnetic field lines and so directed towards the magnetic poles, where an accretion column forms. Often, the rotation axis is different from the magnetic dipole axis. This results in the observed periodical pulsations, comparable to a lighthouse. The pulse profile is then expected to show two main peaks. For GX 304–1, pulse profiles were calculated for XIS for energy bands 1–4 keV, 4–7 keV and 7–10 keV, for PIN for energy bands 10–20 keV, 20–30 keV and 30–50 keV and for GSO for its entire energy range. In Figures 4.2, 4.3 and 4.4 the background subtracted profiles of XIS, PIN and GSO are shown, respectively. The reference time, i.e., where the phase equals zero was set to MJD 55957.437 for all pulse profiles. One remarkable result is that the XIS profiles show not two but three distinct peaks. This already indicates that the accretion geometry and mechanism are far more complex than the simple model of the accreted matter only directed towards the magnetic poles and the X-ray radiation originating from the accretion

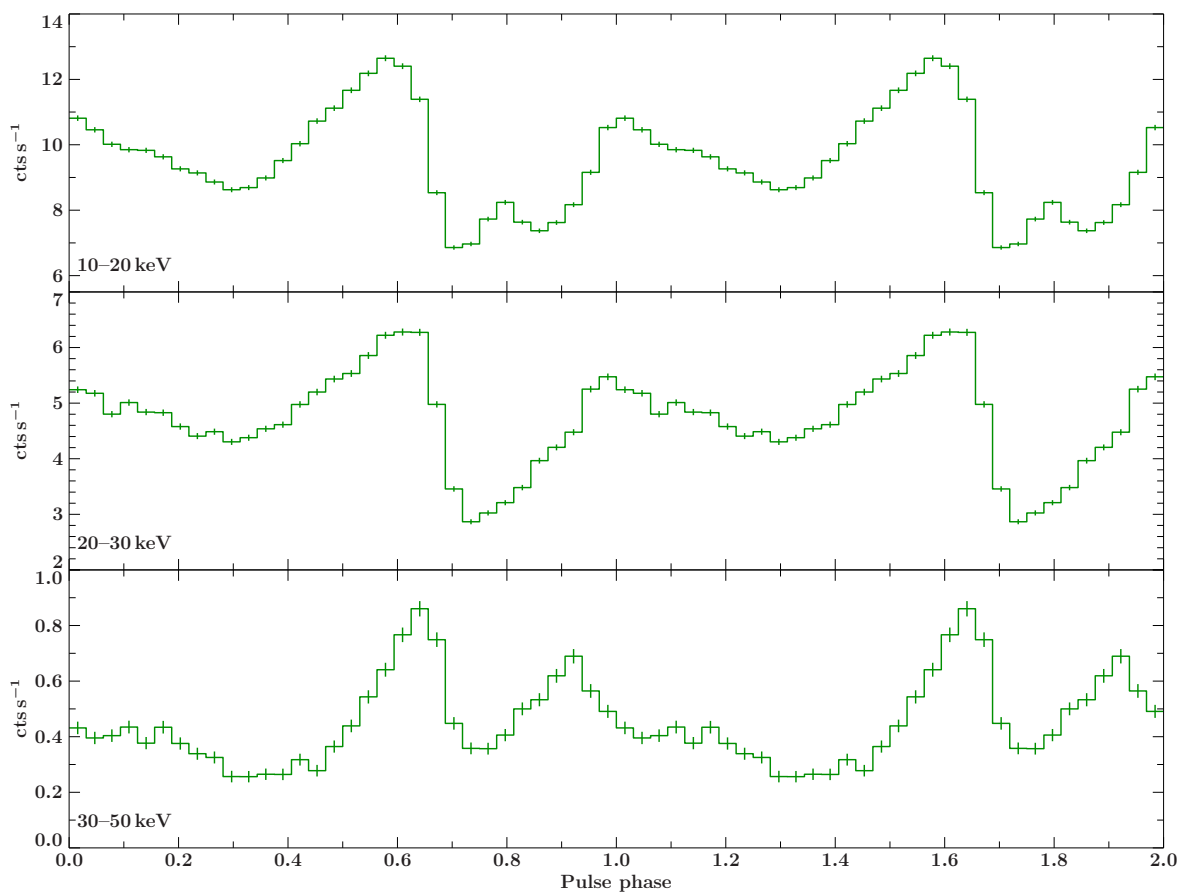


Fig. 4.3.: PIN pulse profiles for different energy bands. Pulse profiles are shown twice for clarity.

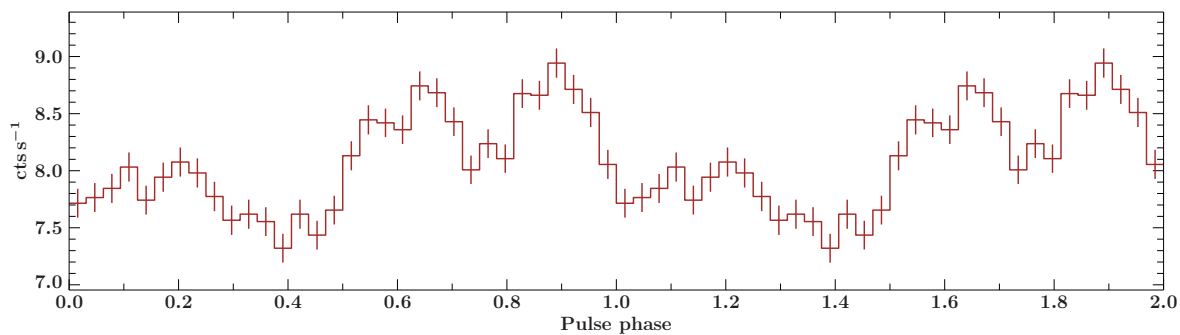


Fig. 4.4.: GSO pulse profile for entire energy range 50–600 keV. Pulse profiles are shown twice for clarity.

columns and hot spots. The relative strength of the individual peaks change between the different energy bands. There are also indications for phase lags, i.e., the hard peaks appear at earlier phase than the hard ones. The higher sensitivity of the back-illuminated XIS1 for soft X-ray radiation is also nicely visible. Apart from that, all XIS0 to XIS3 profiles agree very well. For the higher energy bands, the shape of the pulse profiles change completely. Above 20 keV, one peak vanishes completely and the remaining peaks become broader and less clear. The GSO profile shows also indications of pulsations, though at very low signal to noise ration. The origin of these phase shifts are still highly debated. Simulations show, that relativistic light-tracing effects play an important role in the formation of the pulse profiles and also significant phase shifts at energies around the cyclotron energy have been reported (e.g., Ferrigno et al. 2011). Numerical calculations by Schönherr et al. (2013) showed that phase lags are a result of resonant scattering and angular redistribution of photons around the cyclotron energy. The formation of the pulse profiles is highly dependent on the accretion geometry and observations indicate an asymmetric location of the accretion columns. Unfortunately, the occurrence of phase lags around the cyclotron energy can not be investigated with this data set because of too low S/N. Phase lags are also observable at energies far below the the cyclotron energy, which indicates that also other phenomena contribute to the formation of phase lags. A dependence of the mean photon energy from emission heights has been supposed to cause phase shifts, although Wolfram (2011) predicted the soft peaks to precede the higher ones, which can not be confirmed for this observation. The observed strong energy dependence of the pulse profile concerning both the shape and the phase shifts motivate to study this behaviour in more detail. For this reason, pulse profiles of very narrow energy bands compatible with the resolution of the detectors were extracted with XIS3 and PIN. To deal with the decreasing count rate towards higher energies, the mean count rate was subtracted from each pulse profile and the profile was then divided by its standard deviation. The considered energy range was 1–44 keV because of S/N. The energy resolution of the XIS3 and PIN profiles was set to 0.1 keV and 0.75 keV, respectively. Figure 4.5 shows a color coded map of the count rates as a function of pulse phase and energy. To make the plot more understandable: a vertical cut at a certain phase would give a phase resolved spectrum of that particular phase, whereas a horizontal cut at a certain would produce pulse profile for that given energy band. Again, one observes the disappearance of one peak between 15 keV and 18 keV. The weakest peak in the 1–4 keV band of XIS becomes increasingly strong with higher energy. Phase shifts are of course noticeable, but the individual peaks shift differently. One should also be aware that the apparent merging of the two hard peaks above 35 keV is not significant due to the very low S/N and the two peaks can be recognized in the GSO profile as well. To investigate the evolution of the position of the pulse peaks further, the XIS3 and PIN profiles were fitted with a triple and double Gaussian, respectively, with an additional constant to model background. Figure 4.6 shows an example fit of the XIS3 pulse profile in the 8.0–8.5 keV energy band with three Gaussians. As the third peak vanishes around ~ 18 keV, the PIN profiles were fitted with two Gaussians only. The resulting peak positions are shown in Figure 4.7. The first peak (starting around phase ~ 0.1 , blue data points in Figure 4.7) shows hardly any phase shifts in the energy range 1–10 keV, but significant phase shift at higher energies. The second peak (starting around phase ~ 0.55 , red data points in Figure 4.7) shows phase shifts already at lower energies. The starting position is within the uncertainty intervals up to ~ 25 keV, but

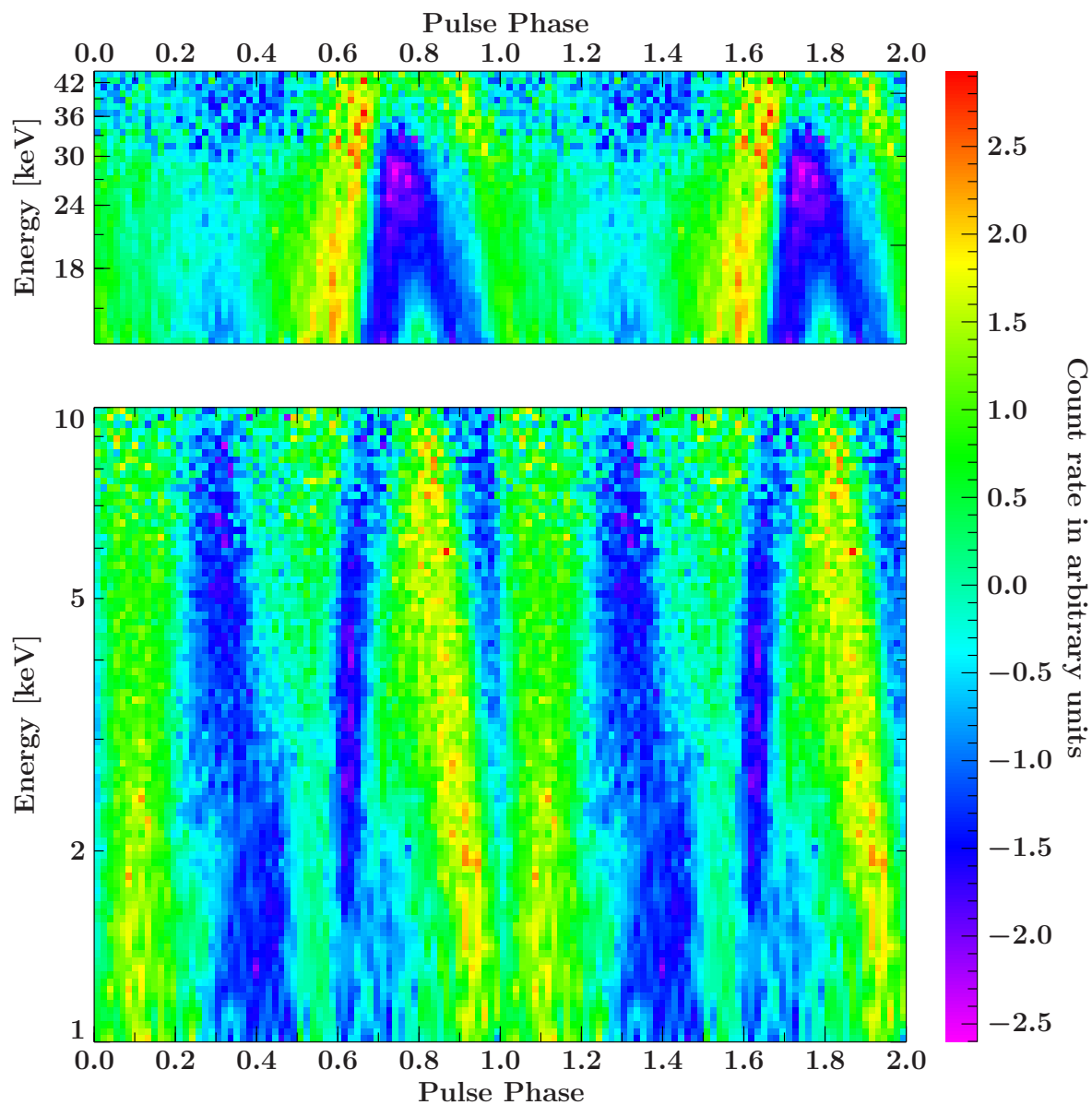


Fig. 4.5.: Color coded map of count rates as a function of pulse phase and energy. All pulse profiles are zero averaged and count rates are in units of standard deviation. Lower panel shows XIS3 profiles, upper panel PIN profiles.

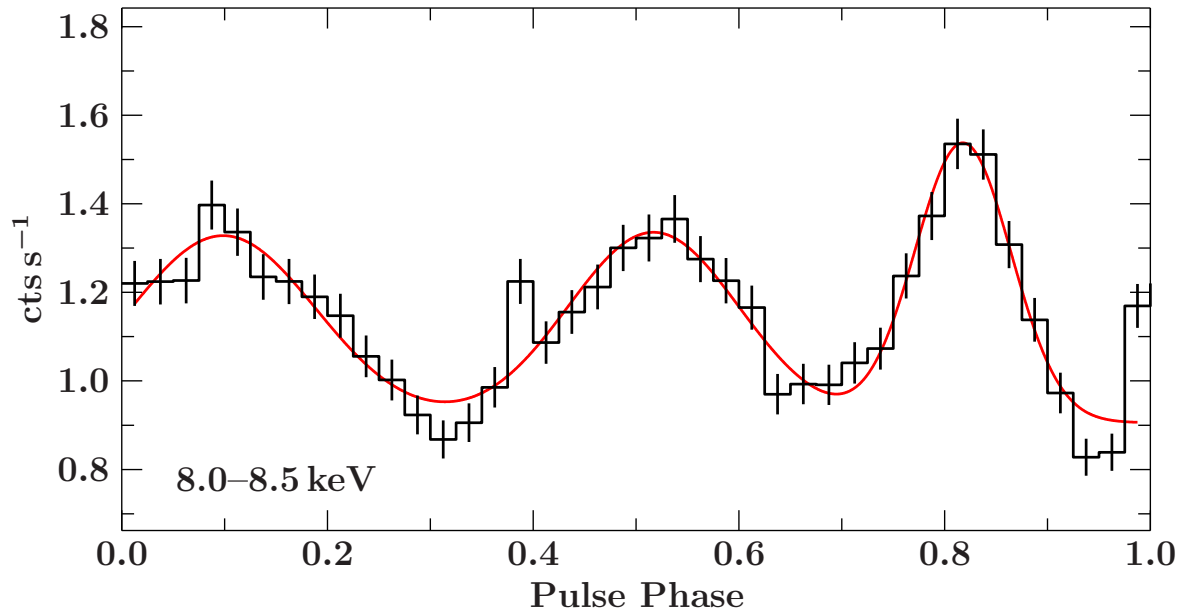


Fig. 4.6.: Fit of the XIS3 profile (black) in the energy band 8.0–8.5 keV with three Gaussians and an additive constant (red) to determine center and width of each peak.

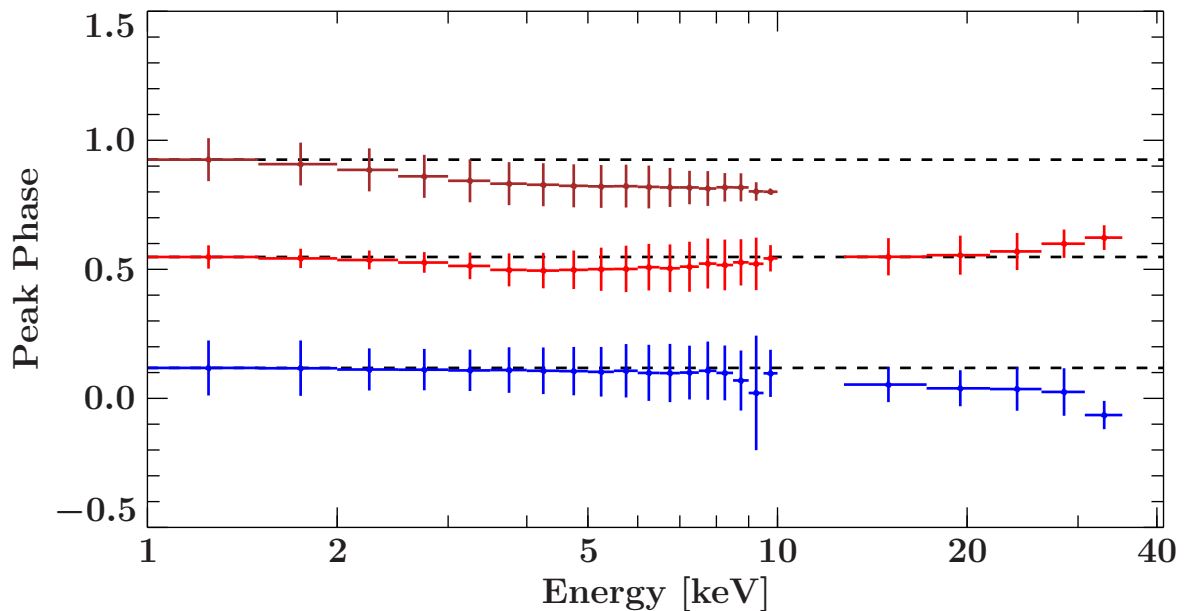


Fig. 4.7.: Phase of the pulse peaks as function of energy, as obtained by fitting the pulse peaks with Gaussians. The third peak (brown) vanishes around ~ 18 keV and thus its position could not be further determined. Bars in y-direction indicate the HWHM of the Gaussians, lines in the x-direction represent the width of the respective energy band. The dashed lines show the phase position of the lowest energy band for each peak.

one should note, that error bars indicate the HWHM of the respective Gaussian, not the usual 90% confidence level. The vanishing third peak (starting around phase ~ 0.9 , brown data points in Figure 4.7) exhibits the most significant phase shift.

5. Spectroscopy

In this section, methods and results of spectral analysis of GX 304–1 are presented. Modelling X-ray spectra is always quite complicated, as several radiation processes contribute to the formation of the observed spectrum. The X-ray emission is powered by the conversion of gravitational energy of the accreted matter to radiation. The X-ray radiation of accretion powered pulsars mainly consists of bremsstrahlung emitted by the incoming plasma that is decelerated inside the accretion column during its fall down to the neutron star's surface. At the bottom of the accretion column, matter is accumulated forming a mound, that is assumed to emit blackbody radiation. Figure 5.1 shows a sketch of gas accreting onto the surface of a neutron star. These mechanisms produce seed photons which gain energy by inverse Compton scattering. Additionally, emission lines, e.g., from iron K_α are often observed. One typical phenomenon of neutron star spectra is the appearance of cyclotron lines. In strong magnetic fields, the momenta of the electrons are quantized in discrete Landau levels. The energy of the Landau levels is given by

$$E_n = m_e c^2 \frac{\sqrt{1 + 2nB/B_{\text{crit}} \sin^2 \theta} - 1}{\sin^2 \theta} \quad (n = 1, 2, 3 \dots), \quad (5.1)$$

where, $m_e c^2$ is the rest energy of the electron, θ the angle between the photon and the magnetic field and B_{crit} is critical magnetic field of $4.4 \cdot 10^{13}$ G (Schönherr et al. 2007a). The transmission of electrons between Landau levels is connected to the emission and absorption of photons of integer multiples of the fundamental Landau energy. These process causes absorption features in the observed spectrum. The detection of cyclotron lines is therefore of great importance, as it allows to measure the magnetic field strength

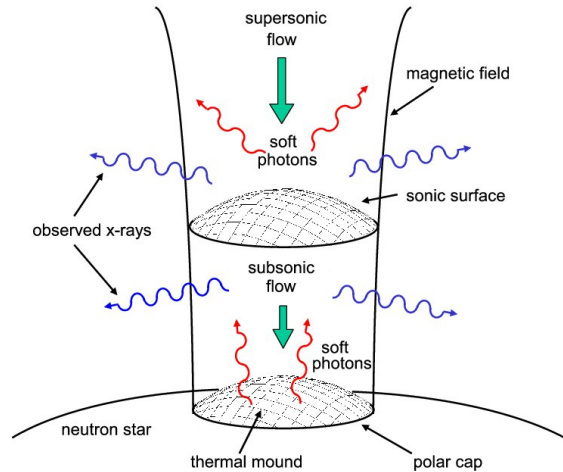


Fig. 5.1.: Sketch of the accretion column. Picture taken from Becker & Wolff (2007).

at the emission region directly over the relation

$$E_{\text{CRSF}} \approx 11.57 \text{ keV} \cdot B_{12} , \quad (5.2)$$

where E_{CRSF} is the energy of the fundamental cyclotron line, which in observations has to be corrected for gravitational redshift and B_{12} is the magnetic field in units of 10^{12} G. However, relativistic and quantum mechanical effects are involved in the cyclotron line formation, so accurate calculations and simulation of the line shape are very challenging. Phenomenological models mostly use Gaussian absorption lines to model cyclotron lines, although the actual line shape is more complex (Harding & Lai 2006; Schönherr et al. 2007b). The photons leaving the accretion column are of course partly absorbed by the interstellar medium. X-ray spectra of accretion powered pulsars are often well described with phenomenological multi-component models. These models include an absorbed powerlaw, often with an exponential cut-off and sometimes additional soft components like blackbody or Comptonization. A disadvantage of these models is that the fitting parameters are not always connected to physical parameters of the source or at least their physical meaning is not completely understood. Remarkable progresses in developing a physical continuum model were made in the last few years (Becker & Wolff 2005, 2007).

5.1. Phase averaged spectroscopy

The phase averaged spectra were extracted in the way described in chapter 3. The continuum is modelled with three different models: a partial coverer, a cut-off powerlaw with an additional blackbody component and the NPEX continuum model. The iron K_{α} and K_{β} lines were added to all of these models and they all require an cyclotron line around 54 keV. The first two models describe the spectrum similarly well, whereas the last does not. All XIS spectra were rebinned to a S/N of 40, PIN to a S/N of 15 and for GSO every 4 channels were binned. The XIS energy range was restricted to 1–10 keV but without 1.72–1.88 keV and 2.19–2.37 keV due to known calibration features. The chosen PIN and GSO energy ranges are 15–60 keV and 70–100 keV, respectively. The Fe K_{α} and K_{β} lines were not fitted individually but the known connection between line energies and fluxes was used. The energy of the K_{β} line was set to $E_{K_{\alpha}} + 0.656$ keV and the flux ratio K_{β}/K_{α} to 0.13 (Kaastra & Mewe 1993). The remaining fitting parameters for the Fe lines are therefore only the K_{α} line energy and flux. The line widths were fixed to the minimum value of $1 \cdot 10^{-6}$, since the broadening of these lines are results of the detector response. All uncertainties given are at the 90% level for one interesting parameter.

5.1.1. Partial coverer

The main component of this model is again a powerlaw with a high energy cut-off, but it is assumed that a fraction of the observed X-ray radiation is again absorbed by the surrounding matter. In ISIS, the corresponding fit function is as follows:

```
constant(Isis_Active_Dataset)*((constant(100)*tbnew_simple(1)
+(1-constant(100))*tbnew_simple(2))*
(cutoffpl(1)*gabs(1)+egauss(1)+egauss(2)))
```

Table 5.1.: Best fit parameters for the partial coverer model.

Parameter name	model component	value
CC XIS0	constant(1).factor	0.9584 ± 0.0029
Cov. Frac	constant(100).factor	0.635 ± 0.012
$N_{H,1}$	tbnew_simple(1).nH	$1.579 \pm 0.023 \times 10^{22} \text{ cm}^{-2}$
$N_{H,2}$	tbnew_simple(2).nH	$9.6 \pm 0.5 \times 10^{22} \text{ cm}^{-2}$
Cont. norm	cutoffpl(1).norm	$0.410^{+0.012}_{-0.010}$
Γ	cutoffpl(1).PhoIndex	0.775 ± 0.017
E_{fold}	cutoffpl(1).HighECut	$14.94^{+0.26}_{-0.24} \text{ keV}$
E_{CRFS}	gabs(1).LineE	$53.7^{+1.4}_{-1.0} \text{ keV}$
σ_{CRFS}	gabs(1).Sigma	$7.2^{+0.9}_{-0.8} \text{ keV}$
A_{CRFS}	gabs(1).Strength	$13.1^{+2.2}_{-1.7}$
A_{Fe}	egauss(1).area	$(1.75 \pm 0.14) \times 10^{-3} \text{ ph s}^{-1} \text{ cm}^{-2}$
E_{Fe}	egauss(1).center	$6.423^{+0.009}_{-0.010} \text{ keV}$
CC XIS01	constant(2).factor	1.016 ± 0.004
CC PIN	constant(4).factor	1.022 ± 0.009
CC GSO	constant(5).factor	0.47 ± 0.07

The first, multiplicative constant takes slightly different normalization of the individual detectors into account. The detector constant of XIS3 was frozen to 1 and the other normalization constants should be very close to this value. The `constant(100)` factor is the coverage fraction, which defines the extent of the partial covering. Absorption columns are modelled with `tbnew_simple` and the Gaussian emission and absorption lines for iron and and the cyclotron line are modelled with the `gabs` and `egauss` components, respectively. The best fit parameters are given in Table 5.1. The $\chi^2/\text{d.o.f} = 1478.09/1114 = 1.33$. A plot of the fitted spectrum is shown in Figure 5.2. The residuals show no significant features. Obviously, GSO has very bad statistics and it is worth considering to completely ignore the GSO data for the spectroscopy. Especially the detector calibration constant of GSO, which should be close to 1 is only 0.47. However, because there are pulsations visible in the GSO profile, this data set was included to all spectral analysis but one must be aware that this affects the final χ^2 values. Nevertheless, the partial coverer gives a satisfactory description of the spectrum and the cyclotron line energy is in agreement with previous observations. This model was also used by Devasia et al. (2011).

5.1.2. Cut-off powerlaw with blackbody

The second continuum model used to fit the phase averaged spectrum is an absorbed powerlaw with an additional blackbody component. The blackbody component is necessary to get a sufficient agreement of model and data in the soft energy range. The fit function in ISIS is defined as:

```
constant(Isis_Active_Dataset)*tbnew_simple(1)*
(cutoffpl(1)+egauss(1)+egauss(2)+bbbody(1))*gabs(1)
```

The best fit parameters are listed in Table 5.2 with $\chi^2/\text{d.o.f} = 1563.88/1114 = 1.40$. The reduced χ^2 value is slightly worse than the one obtained with the partial coverer model but still acceptable. The partial covering geometry can therefore not be confirmed. On the other hand, the soft component of the spectrum that is well described

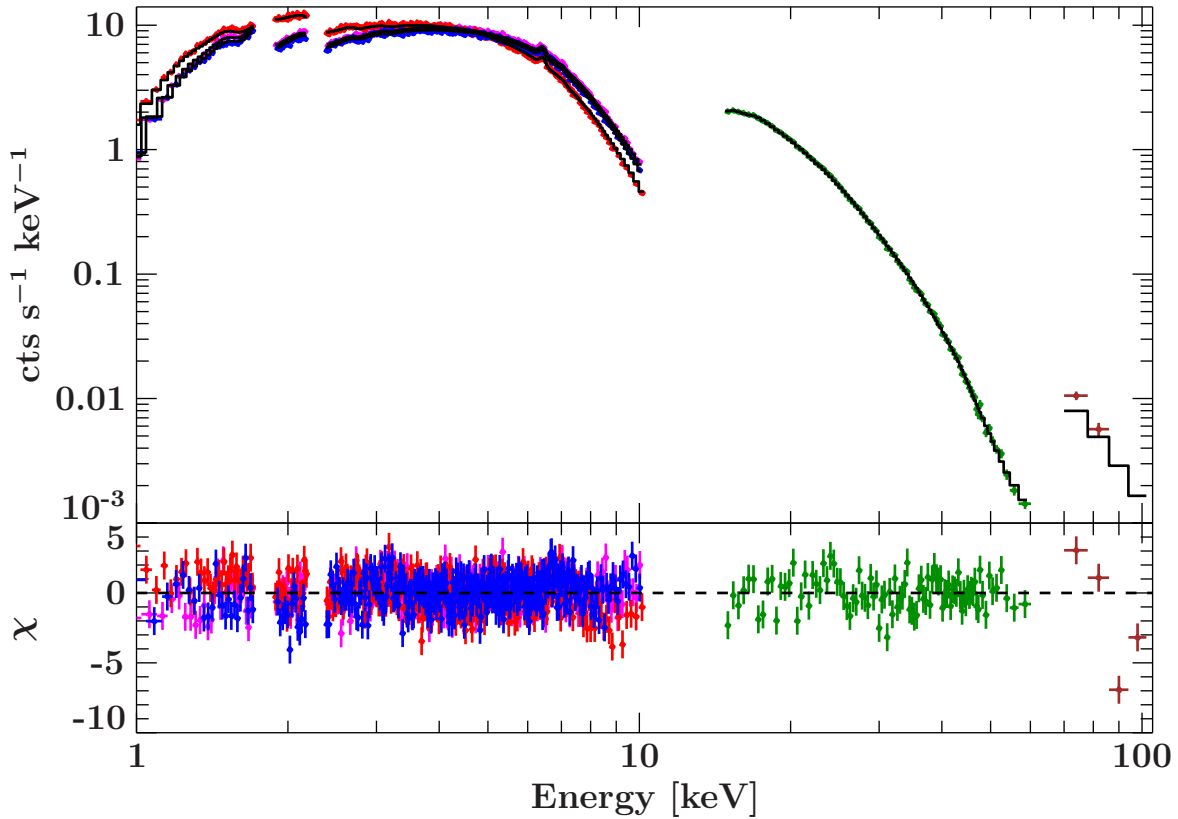


Fig. 5.2.: Phase averaged spectrum with best fit of partial coverer model. XIS0 (blue), XIS1 (red), XIS3 (magenta), PIN (green) and GSO (brown).

by the blackbody component is probably not the radiation emitted from the thermal mound at the polar caps. Figure 5.3 shows the best fit of the spectrum. Again the residuals are flat. The cyclotron line energies of the partial coverer and the blackbody model agree within the confidence levels and the N_{H} is close to the galactic value of $1.06 \times 10^{22} \text{ cm}^{-2}$.

5.1.3. NPEX continuum model

Another empirical way to model the soft X-ray component is a combination of two powerlaws with a positive and negative photon index, all together with a high energy cut-off. Although this model was applied successfully by Yamamoto et al. (2011) to data obtained during the outburst of 2010 August, it failed to describe this dataset properly. The NPEX model is not pre-defined in ISIS and has to be built via:

```
constant(Isis_Active_Dataset)*tbnew_simple(1)*
(cutoffpl(1)+cutoffpl(2)+egauss(1)+egauss(2))*gabs(1)
```

The folding energies of the two cut-off powerlaws were tied together, so the spectrum is effectively fitted with only one folding energy parameter. When fitting the spectrum, the negative photon index immediately reaches its lower limit of -2 and was therefore frozen to that value. The result of the best fit is then $\chi^2/\text{d.o.f} = 2438.76/1115 = 2.19$. The best fit parameters are given in Table 5.3 and a plot of the spectrum is shown in Figure 5.4. From the residuals one can see that NPEX continuum fails to model the soft part of the spectrum between 1 keV and 3 keV. Additionally, some irregularities

Table 5.2.: Best fit parameters for the cut-off powerlaw and blackbody model.

Parameter name	model component	value
CC XIS0	constant(1).factor	0.9584 ± 0.0029
N_{H}	tbnew_simple(1).nH	$1.294^{+0.025}_{-0.026} \times 10^{22} \text{ cm}^{-2}$
Cont. norm	cutoffpl(1).norm	0.154 ± 0.006
Γ	cutoffpl(1).PhoIndex	$0.332^{+0.026}_{-0.027}$
E_{fold}	cutoffpl(1).HighECut	$11.63 \pm 0.20 \text{ keV}$
E_{CRFS}	gabs(1).LineE	$52.4^{+1.2}_{-1.0} \text{ keV}$
σ_{CRFS}	gabs(1).Sigma	$5.4^{+0.8}_{-0.7} \text{ keV}$
A_{CRFS}	gabs(1).Strength	$7.3^{+1.4}_{-1.2}$
A_{Fe}	egauss(1).area	$(1.69 \pm 0.14) \times 10^{-3} \text{ ph s}^{-1} \text{ cm}^{-2}$
E_{Fe}	egauss(1).center	$6.424^{+0.009}_{-0.010} \text{ keV}$
BB. norm	bbody(1).norm	0.0139 ± 0.0008
kT	bbody(1).kT	$1.59 \pm 0.05 \text{ keV}$
CC XIS01	constant(2).factor	$1.0157^{+0.0031}_{-0.0030}$
CC PIN	constant(4).factor	$1.055^{+0.020}_{-0.019}$
CC GSO	constant(5).factor	0.76 ± 0.10

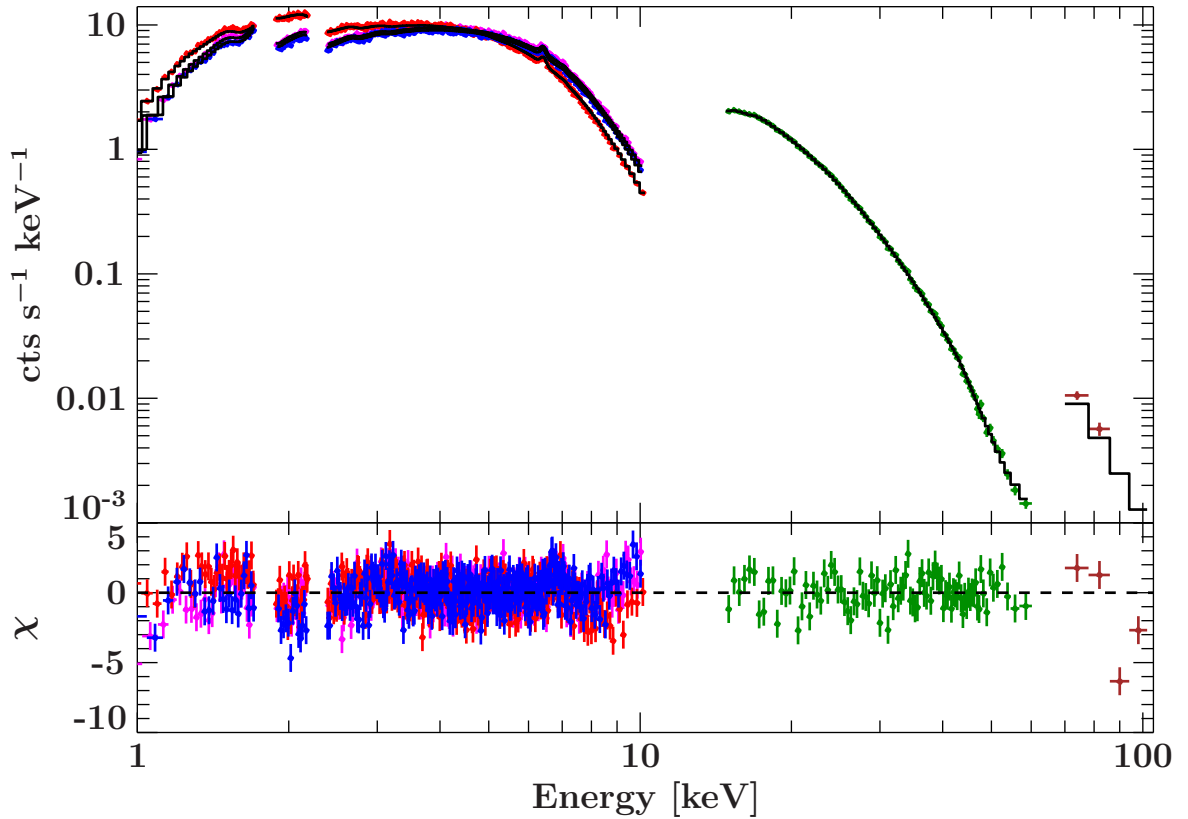
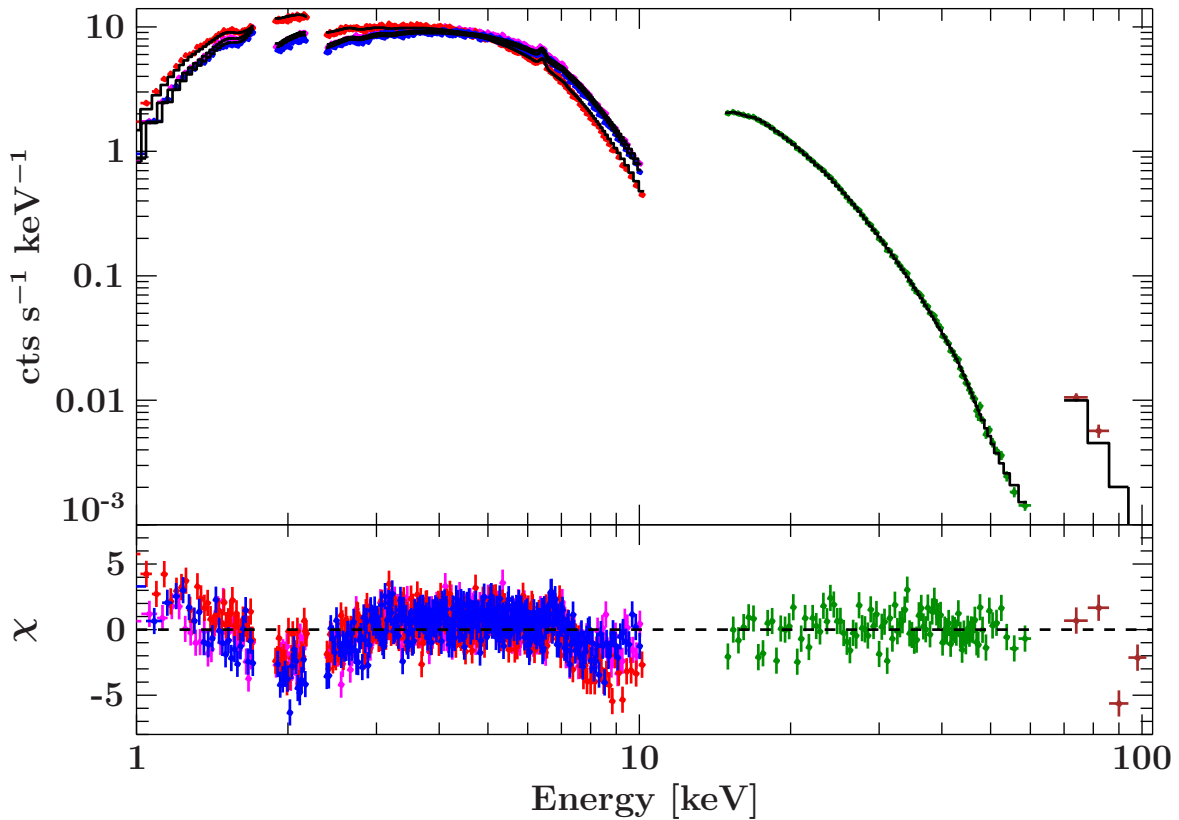
**Fig. 5.3.:** Phase averaged spectrum with best fit of cut-off powerlaw with blackbody continuum model. XIS0 (blue), XIS1 (red), XIS3 (magenta), PIN (green) and GSO (brown).

Table 5.3.: Best fit parameters for the NPEX continuum model.

Parameter name	model component	value
CC XIS0	constant(1).factor	0.9584 ± 0.0029
N_{H}	tbnew_simple(1).nH	$1.522 \pm 0.012 \times 10^{22} \text{ cm}^{-2}$
pos. cont. norm	cutoffpl(1).norm	0.2283 ± 0.0018
neg. cont. norm	cutoffpl(2).norm	$(1.51^{+0.16}_{-0.15}) \times 10^{-4}$
Γ	cutoffpl(1).PhoIndex	$0.273^{+0.008}_{-0.007}$
E_{fold}	cutoffpl(1).HighECut	$7.47^{+0.13}_{-0.12}$
E_{CRFS}	gabs(1).LineE	$51.2^{+1.4}_{-1.2} \text{ keV}$
σ_{CRFS}	gabs(1).Sigma	$4.5^{+0.9}_{-0.8} \text{ keV}$
A_{CRFS}	gabs(1).Strength	$4.7^{+1.2}_{-1.0}$
A_{Fe}	egauss(1).area	$(1.72 \pm 0.14) \times 10^{-3} \text{ ph s}^{-1} \text{ cm}^{-2}$
E_{Fe}	egauss(1).center	$6.420^{+0.010}_{-0.009} \text{ keV}$
CC XIS01	constant(2).factor	1.015 ± 0.004
CC PIN	constant(4).factor	0.972 ± 0.008
CC GSO	constant(5).factor	1.07 ± 0.15

**Fig. 5.4.:** Phase averaged spectrum with best fit of NPEX continuum model. XIS0 (blue), XIS1 (red), XIS3 (magenta), PIN (green) and GSO (brown).

around 9 keV are visible. These problems, together with the large χ^2 value, lead to a rejection of this continuum model.

5.2. Phase resolved spectroscopy

5.2.1. Extraction of phase resolved spectra

Due to the rotation of the neutron star, every pulse phase is connected to a certain viewing angle. The asymmetric accretion geometry makes it obvious, that the spectral shape should depend on this viewing angle. This is the motivation for phase resolved spectroscopy. For that purpose, spectra of specified phase intervals are extracted. For *Suzaku*, this is done by use of additional *Good-Time-Intervals* (GTI) files. GTIs are also a fundamental part of phase averaged spectroscopy. These files contain time intervals that are used to filter the event files, i.e., only events are registered that happened within a GTI, and are also important to calculate the effective exposure time. GTI files are therefore always an extension of the basic event files and internally used by the extraction software. The additional GTI files used for the extraction of phase resolved spectra now contain only time intervals that represent a certain phase interval. Assuming, that the pulse period p does not change during the observation, these time intervals are simply calculated by

$$t_{\text{start},k} = t_0 + kp\phi_{\text{start}} \quad (5.3)$$

$$t_{\text{stop},k} = t_0 + kp\phi_{\text{stop}}, \quad (5.4)$$

where t_0 is a reference time where the phase equals zero, $\phi_{\text{start/stop}}$ the beginning and end of the phase interval and $k \in \mathbb{Z}$ is to be chosen such that $t_{\text{start},k}$ and $t_{\text{stop},k}$ match the time of observation. It is important to note that the times calculated this way refer to the barycentric system of reference. The *Suzaku* data extraction software, however, requires the GTIs to refer to the satellite's local system of reference. For this reason, all calculated GTIs have to be converted to the local system. The tool `aebarycen` can only convert times from the local to barycentric system, but not the other way round. This can be achieved by using two identical event files, one in the local and one in the barycentric system and interpolating the GTIs in the local system from the event times. The default barycentric correction, that is part of the standard extraction routines can be skipped optionally and thus the two event files can be easily generated. In this case, the PIN event file was used because of its high time resolution and only one observation mode. Eight equally spaced phase intervals were selected as shown in Figure 5.5. The phase resolved spectra were rebinned with slightly different binning than the phase averaged spectra. The XIS spectra were rebinned to a S/N of 35, PIN to a S/N of 10 and for GSO again every 4 channels were binned. The partial coverer and blackbody model, which proved successful for the phase averaged spectrum should also hold for the phase resolved spectra as well. However, this seems not to be the case.

5.2.2. Partial coverer and blackbody model

First, the partial coverer model as defined in section 5.1.1 was fitted to all spectra individually without any further constraints. The best fit parameters, however, disagree with physical assumptions. For example, the folding energy, which is supposed to be connected to the finite bulk velocity of the accretion column and should therefore not depend on the pulse phase was observed to vary between ~ 10 keV and ~ 25 keV. An even more severe problem is the variation of the detector calibration constants, which take

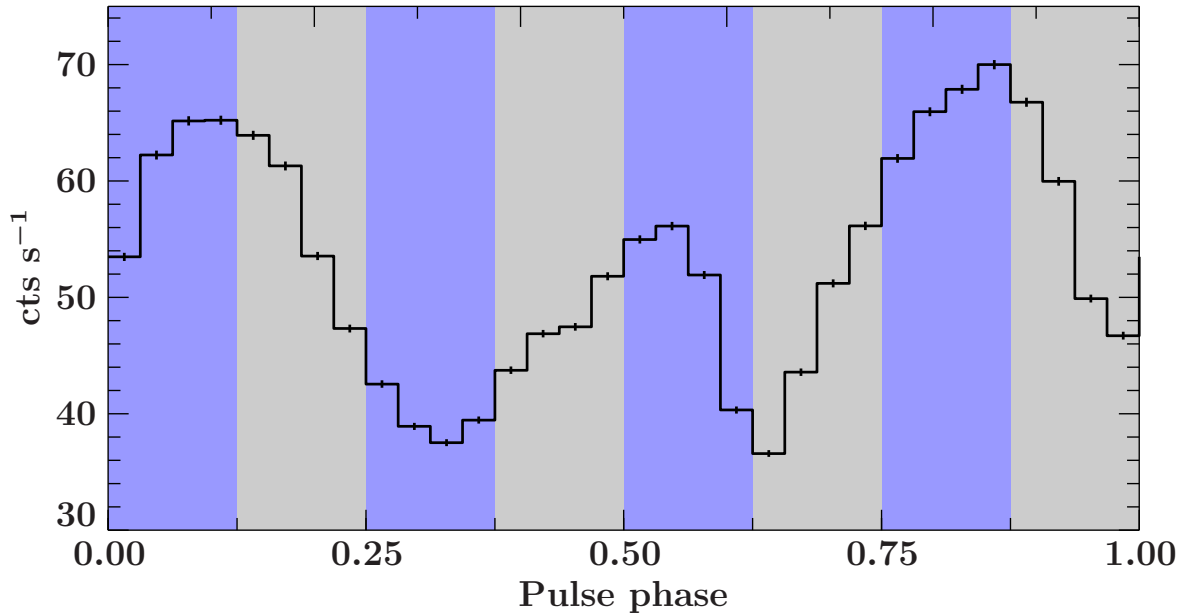


Fig. 5.5.: Pulse profile of XIS3 for energy range 1-10 keV. The blue and grey shaded regions indicate the intervals for phase resolved spectroscopy.

care of slightly different normalization and are thus model parameters concerning only the detector. These parameters have thus to be constant within the uncertainty levels. Similar problems occurred for blackbody model. Due to these problems, the attempt to fit the phase resolved spectra independently was abandoned early. The spectra were then fitted simultaneously where some parameters are declared *global*, i.e., are the same for each spectrum, while others are fitted separately. In a first approach, only the detector constants were declared global parameters. This however resulted partly in negative photon indices, which have no physical interpretation. On the other hand, a strong correlation between the photon index and the folding energy is observed (see Figure 5.6) and also plausible. Therefore, the model was further restricted and also the folding energy was declared global for the reason mentioned above. The partial coverer and the blackbody model were then both fitted simultaneously to all phase intervals. Now this ensures positive photon indices but the fit results are still not very satisfying. Figures 5.7 and 5.9 show the best fits with the partial coverer and the blackbody continuum model, respectively. The overall reduced χ^2 of the partial coverer is 2.33 and the one of the blackbody continuum model is 1.73. Interestingly, the blackbody continuum model gives the better description of the phase resolved spectra. Some phases can be well described with both models (e.g., phase 0.125–0.25), while others show strong irregularities in the residuals (e.g., phase 0.625–0.75). An additional feature between 20 keV and 30 keV can be observed with both models for phases 0.5–0.625 and 0.625–0.75 and for the blackbody model also for 0.375–0.5 and 0.75–0.875. Another important observation concerns the modelling of the cyclotron line. Constraining the parameters of the cyclotron line turned out to be very difficult and not always possible. For several phases the width of the cyclotron line hit its upper limit of 10 keV and also once the lower limit of 0 keV. However, the ranges have not been widened to avoid modelling the continuum with the absorption feature, as shown by Müller et al. (2012). Uncertainty calculations of these parameters are also not possible. One should therefore be very cautious to draw any conclusions from these values. The

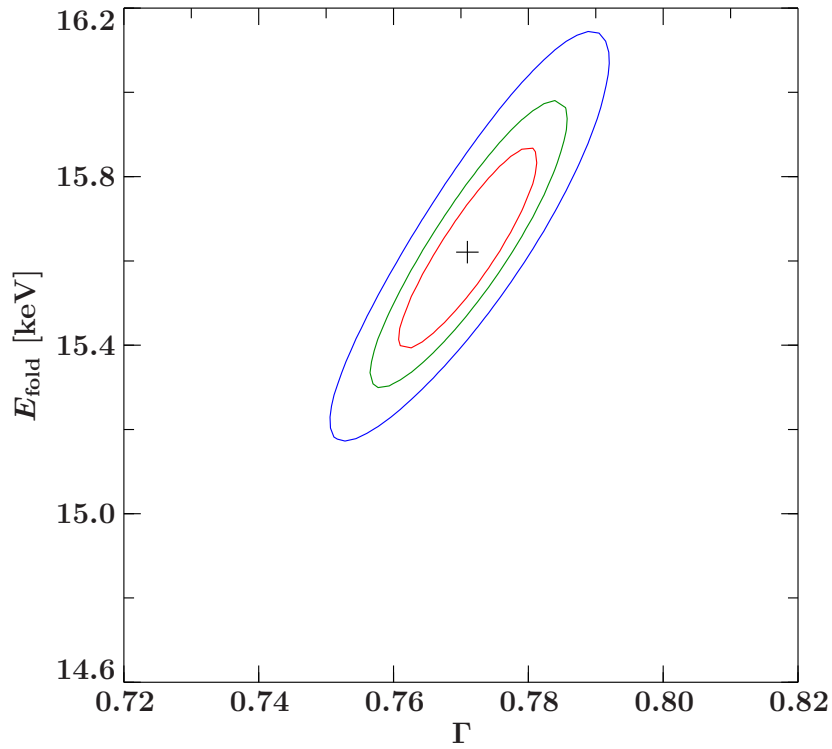


Fig. 5.6.: Confidence contours for folding energy and photon index for the phase averaged spectrum, fitted with partial coverer. Contour lines correspond to the 68.3%, 90%, and 99% level

same problem occurred for the partial coverer model for the coverage fraction and some N_{H} values. The critical values were frozen, although this is not absolutely statistically correct and affects the uncertainties of the other parameters. The evolution of the parameters are shown for both models in Figures 5.8 and 5.10. All best fit parameters are listed in appendices A and B, where also the frozen parameters are marked. The essential conclusion is that the models successful for the phase averaged spectra cannot provide a proper description of all phase resolved spectra.

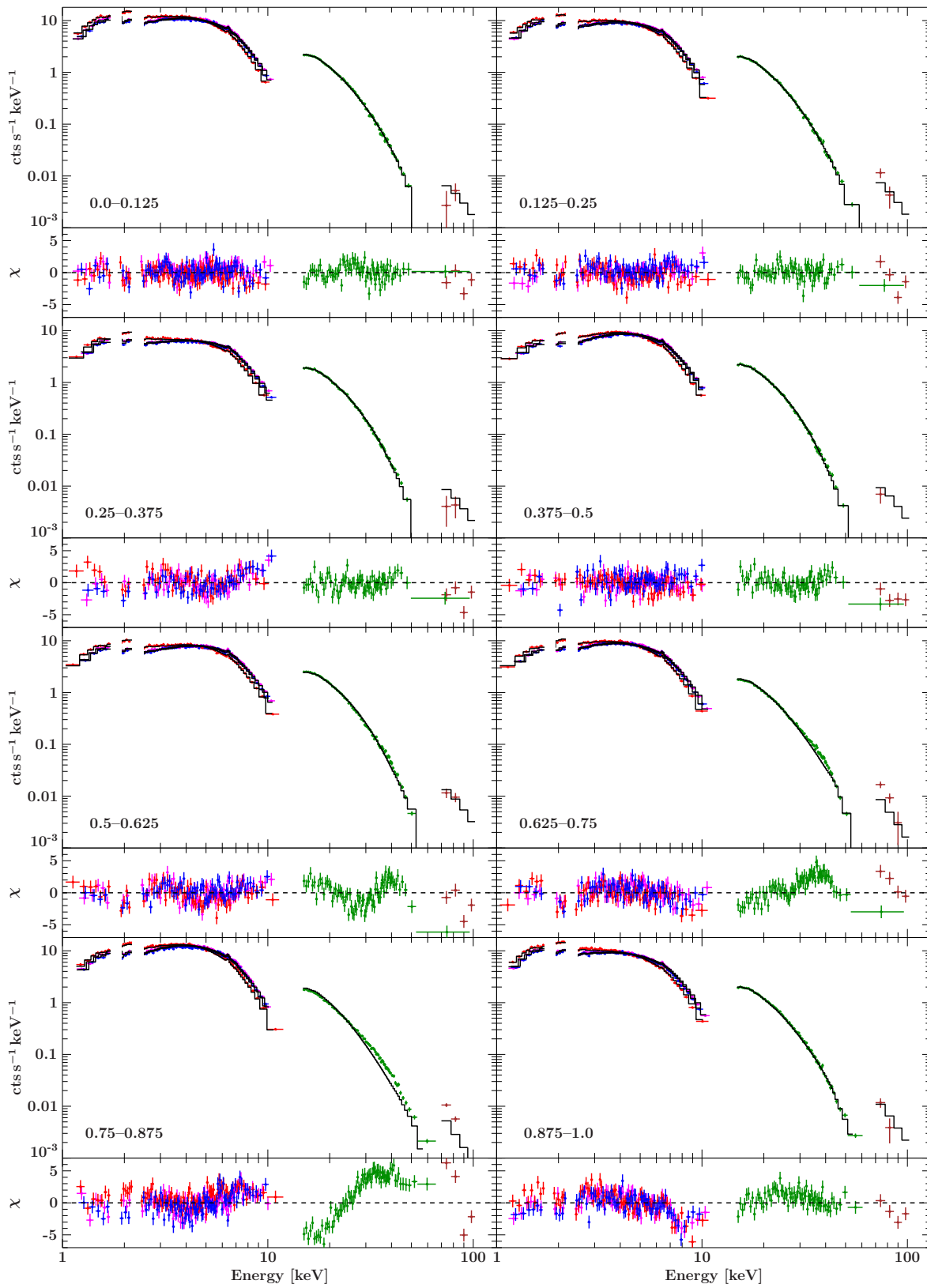


Fig. 5.7.: Best fit of phase resolved spectra with partial coverer. XIS0 (blue), XIS1 (red), XIS3 (magenta), PIN (green) and GSO (brown).

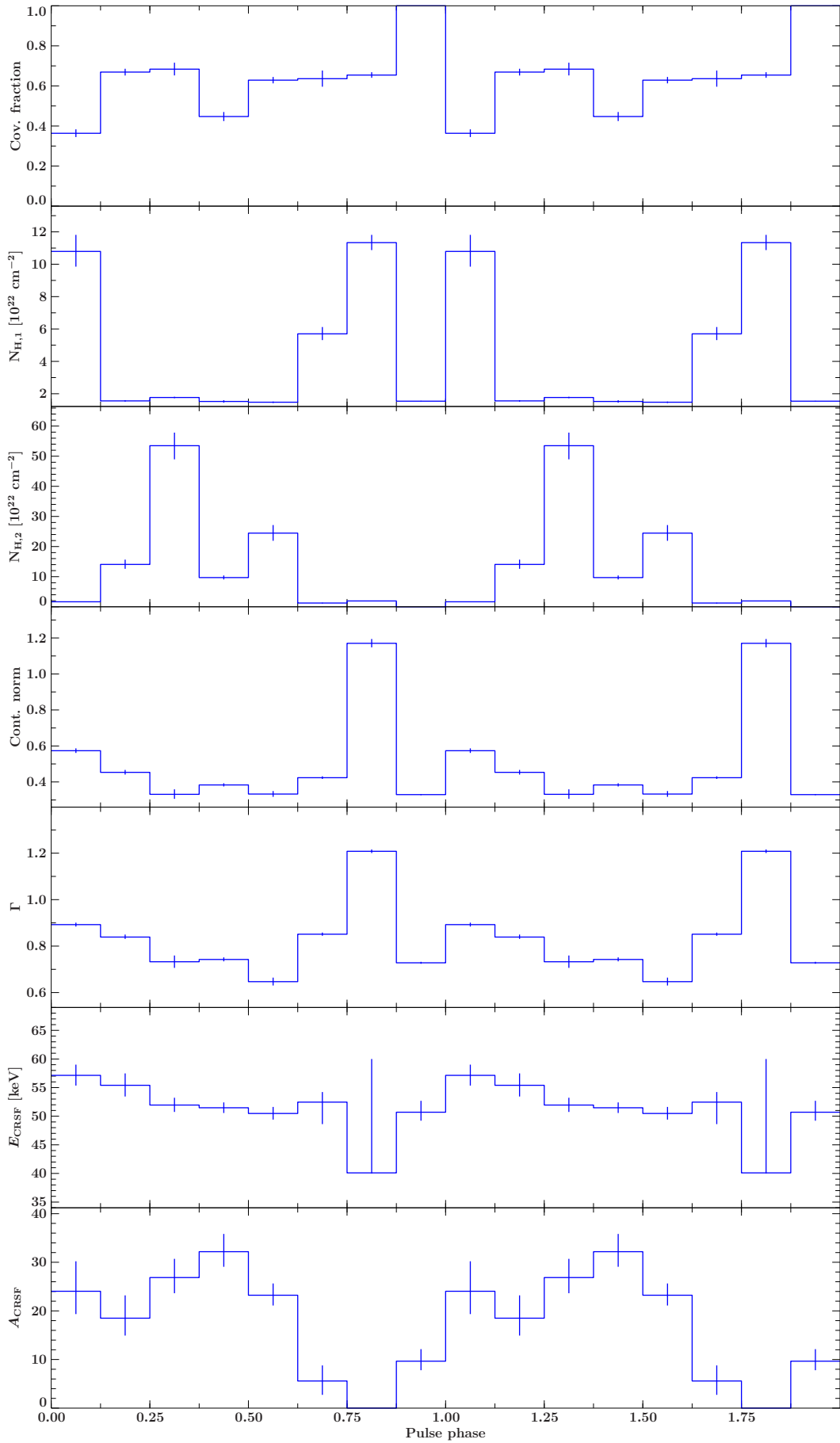


Fig. 5.8.: Evolution of fit parameters of partial coverer. The cyclotron line energy E_{CRFS} for phase 0.75–0.875 is not valid, as the strength of the line had to be frozen to zero. Here, errors represent the given limits of the line energy.

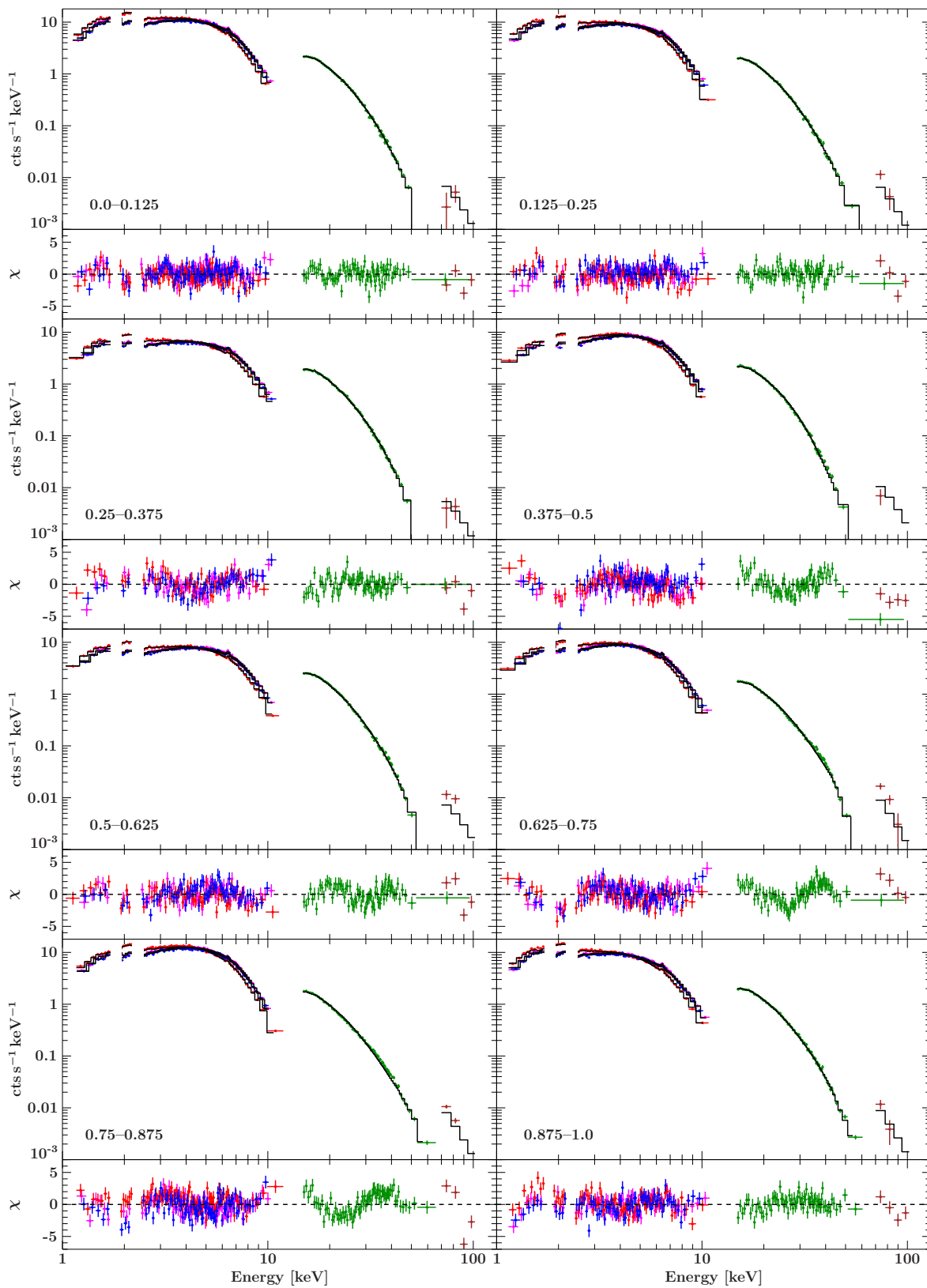


Fig. 5.9.: Best fit of phase resolved spectra with blackbody model. XIS0 (blue), XIS1 (red), XIS3 (magenta), PIN (green) and GSO (brown).

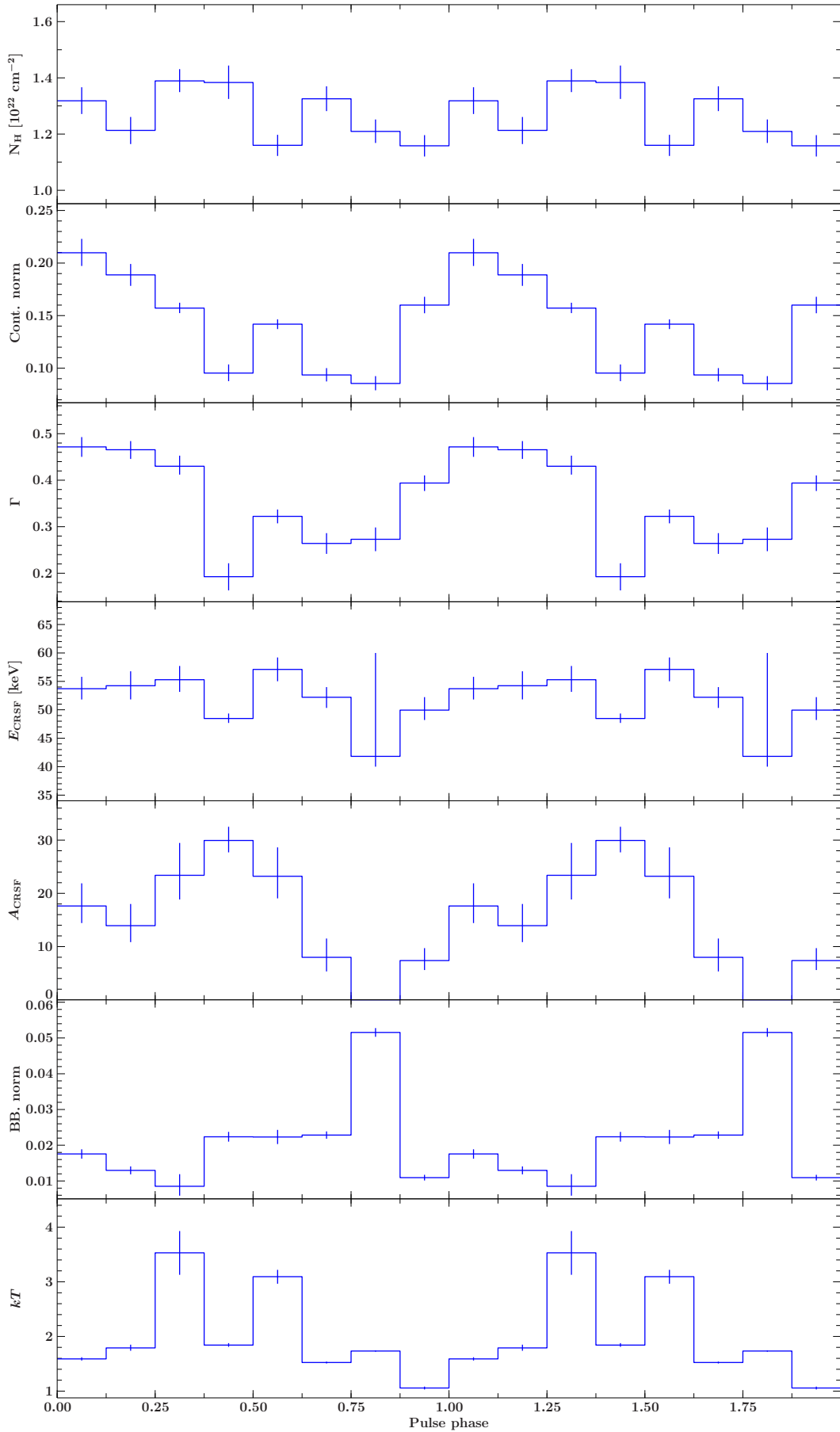


Fig. 5.10.: Evolution of fit parameters of blackbody model. The cyclotron line energy E_{CRFS} for phase 0.75–0.875 is not valid, as the other parameters of the line are frozen to zero. Here, errors represent the given limits of the line energy.

6. Conclusions

The *Suzaku* data of the 2012 January outburst of GX 304–1 was analysed for timing and spectral characteristics. The detected pulse period is in agreement with previous observations, but also confirms changes of the pulse period over time. The pulse profiles show a three peak structure in the low energy band which evolves to two peaks towards higher energies. The complex structure of the pulse profile was already reported by Devasia et al. (2011), who also observed a variation of the pulse profile during the outburst. Unfortunately, there is only one *Suzaku* observation of this outburst available, so this could not be investigated. However, there is an earlier *Suzaku* observation from 2010 August that might be worthwhile to compare with these results. Phaselags have also been detected for this source. The origin of this phenomenon is still highly debated. The low S/N does not allow to study the phaselags in the energy range around the cyclotron line, but this is definitely worth trying with other satellites, as simulations suggest a strong connection of phaseshifts to cyclotron resonant scattering. The spectral analysis confirms the presence of a cyclotron line around 54 keV as reported by Yamamoto et al. (2011). However, reliable parameters of the cyclotron line can only be constrained for the phase averaged spectrum. The empirical models fail to provide a satisfying description of the phase resolved spectra. It is therefore necessary to consider other continuum models. Testing the self-consistent Becker & Wolff hybrid model (Becker & Wolff 2007) on the phase resolved spectra should be the next step of spectral analysis. It was successfully applied by Ferrigno et al. in 2009 to 4U 0115+63. This might be also promising for GX 304–1. Phase resolved spectroscopy of other satellites of this source might give further insights on the problems of the continuum modelling, too.

References

- Becker, P. A., Klochkov, D., Schönherr, G., et al. 2012, *A&A*, 544, A123
- Becker, P. A. & Wolff, M. T. 2005, *ApJ*, 630, 465
- Becker, P. A. & Wolff, M. T. 2007, *ApJ*, 654, 435
- Davis, J. E. 2001, *ApJ*, 562, 575
- Devasia, J., James, M., Paul, B., & Indulekha, K. 2011, *MNRAS*, 417, 348
- Ferrigno, C., Becker, P. A., Segreto, A., Mineo, T., & Santangelo, A. 2009, *A&A*, 498, 825
- Ferrigno, C., Falanga, M., Bozzo, E., et al. 2011, *A&A*, 532, A76
- Friedman, H., Lichtman, S. W., & Byram, E. T. 1951, *Phys. Rev.*, 83, 1025
- Fukazawa, Y., Mizuno, T., Watanabe, S., et al. 2009, *PASJ*, 61, 17
- Giacconi, R., Branduardi, G., Briel, U., et al. 1979, *ApJ*, 230, 540
- Giacconi, R., Gursky, H., Paolini, F. R., & Rossi, B. B. 1962, *Phys. Rev. Lett.*, 9, 439
- Harding, A. K. & Lai, D. 2006, *Reports on Progress in Physics*, 69, 2631
- Huckle, H. E., Mason, K. O., White, N. E., et al. 1977, *MNRAS*, 180, 21P
- Kaastra, J. S. & Mewe, R. 1993, *A&AS*, 97, 443
- Klochkov, D., Doroshenko, V., Santangelo, A., et al. 2012, *A&A*, 542, L28
- Koyama, K., Tsunemi, H., Dotani, T., et al. 2007, *PASJ*, 59, 23
- Leahy, D. A., Darbro, W., Elsner, R. F., et al. 1983, *ApJ*, 266, 160
- Lewin, W. H. G., Clark, G. W., & Smith, W. B. 1968, *ApJ*, 152, L49
- Mason, K. O., Murdin, P. G., Parkes, G. E., & Visvanathan, N. 1978, *MNRAS*, 184, 45P
- McClintock, J. E., Nugent, J. J., Li, F. K., & Rappaport, S. A. 1977, *ApJ*, 216, L15
- Mitsuda, K., Bautz, M., Inoue, H., et al. 2007, *PASJ*, 59, 1
- Müller, S., Kühnel, M., Caballero, I., et al. 2012, *A&A*, 546, A125
- Pietsch, W., Oegelman, H., Kahabka, P., Collmar, W., & Gottwald, M. 1986, *A&A*, 163, 93

- Priedhorsky, W. C. & Terrell, J. 1983, *ApJ*, 273, 709
- Rothschild, R. E., Blanco, P. R., Gruber, D. E., et al. 1998, *ApJ*, 496, 538
- Schönherr, G., Schwarm, F.-W., Falkner, S., et al. 2013, *A&A*, in press
- Schönherr, G., Wilms, J., Kretschmar, P., et al. 2007a, in *ESA Special Publication*, Vol. 622, *ESA Special Publication*, 457
- Schönherr, G., Wilms, J., Kretschmar, P., et al. 2007b, *A&A*, 472, 353
- Takahashi, T., Abe, K., Endo, M., et al. 2007, *PASJ*, 59, 35
- Uchiyama, Y., Maeda, Y., Ebara, M., et al. 2008, *PASJ*, 60, 35
- van der Klis, M. 1989, in *Timing Neutron Stars*, ed. H. Ögelman & E. P. J. van den Heuvel, 27
- Voges, W., Aschenbach, B., Boller, T., et al. 1999, *A&A*, 349, 389
- Wolfram, K. D. 2011, *Dissertation*, George Mason University
- Wolter, H. 1952, *Ann. Phys.*, 445, 94–114
- Yamamoto, T., Nakahira, S., Kawai, N., et al. 2009, *The Astronomer's Telegram*, 2297, 1
- Yamamoto, T., Sugizaki, M., Mihara, T., et al. 2011, *PASJ*, 63, 751

A. Best fit parameters of phase resolved spectra with partial coverer

Table A.1.: Best fit parameters of the global parameters with partial coverer. * denotes a value that was frozen because of limit violation.

Table A.2.: Best fit parameters of phase 0.0–0.125 with partial coverer. * denotes a value that was frozen because of limit violation.

Table A.3.: Best fit parameters of phase 0.125–0.25 with partial coverer. * denotes a value that was frozen because of limit violation.

Table A.4.: Best fit parameters of phase 0.25–0.375 with partial coverer. * denotes a value that was frozen because of limit violation.

Table A.5.: Best fit parameters of phase 0.375–0.5 with partial coverer. * denotes a value that was frozen because of limit violation.

Table A.6.: Best fit parameters of phase 0.5–0.625 with partial coverer. * denotes a value that was frozen because of limit violation.

Table A.7.: Best fit parameters of phase 0.625–0.75 with partial coverer. * denotes a value that was frozen because of limit violation.

Table A.8.: Best fit parameters of phase 0.75–0.875 with partial coverer. * denotes value that was frozen because of limit violation. The cyclotron line energy E_{CRFS} is not valid, as the other parameters of the line are frozen to zero. Errors represent the given limits of the line energy.

Table A.9.: Best fit parameters of phase 0.875–1.0 with partial coverer. * denotes value that was frozen because of limit violation.

Global parameter name	model component	value
CC XIS0	constant(1).factor	0.9583 ± 0.0020
CC XIS1	constant(2).factor	0.9903 ± 0.0020
CC PIN	constant(4).factor	1.041 ± 0.006
CC GSO	constant(5).factor	0.500*
E_{fold}	cutoffpl(1).HighECut	15.52 ± 0.06 keV

Parameter name	model component	value
Cov. Frac	constant(100).factor	$0.364^{+0.020}_{-0.019}$
$N_{H,1}$	tbnew_ simple(1).nH	$10.8 \pm 1.0 \times 10^{22} \text{ cm}^{-2}$
$N_{H,2}$	tbnew_ simple(2).nH	$1.66^{+0.05}_{-0.06} \times 10^{22} \text{ cm}^{-2}$
Cont. norm	cutoffpl(1).norm	0.574 ± 0.013
Γ	cutoffpl(1).PhoIndex	0.892 ± 0.009
E_{CRFS}	gabs(1).LineE	$57.1^{+1.9}_{-1.8} \text{ keV}$
σ_{CRFS}	gabs(1).Sigma	10 keV*
A_{CRFS}	gabs(1).Strength	24^{+7}_{-5}
A_{Fe}	egauss(1).area	$(2.0 \pm 0.4) \times 10^{-3} \text{ ph s}^{-1} \text{ cm}^{-2}$
E_{Fe}	egauss(1).center	$6.428^{+0.024}_{-0.020} \text{ keV}$
$\chi^2/\text{d.o.f} = 433.27/341 = 1.27$		

Parameter name	model component	value
Cov. Frac	constant(100).factor	0.669 ± 0.017
$N_{H,1}$	tbnew_ simple(1).nH	$1.56 \pm 0.05 \times 10^{22} \text{ cm}^{-2}$
$N_{H,2}$	tbnew_ simple(2).nH	$14.1^{+1.7}_{-1.5} \times 10^{22} \text{ cm}^{-2}$
Cont. norm	cutoffpl(1).norm	$0.453^{+0.014}_{-0.013}$
Γ	cutoffpl(1).PhoIndex	$0.839^{+0.010}_{-0.008}$
E_{CRFS}	gabs(1).LineE	$55.4 \pm 2.0 \text{ keV}$
σ_{CRFS}	gabs(1).Sigma	10 keV*
A_{CRFS}	gabs(1).Strength	19^{+5}_{-4}
A_{Fe}	egauss(1).area	$(1.5 \pm 0.4) \times 10^{-3} \text{ ph s}^{-1} \text{ cm}^{-2}$
E_{Fe}	egauss(1).center	$6.42^{+0.05}_{-0.04} \text{ keV}$
$\chi^2/\text{d.o.f} = 403.17/307 = 1.31$		

Parameter name	model component	value
Cov. Frac	constant(100).factor	0.68 ± 0.04
$N_{H,1}$	tbnew_ simple(1).nH	$1.77 \pm 0.05 \times 10^{22} \text{ cm}^{-2}$
$N_{H,2}$	tbnew_ simple(2).nH	$53 \pm 5 \times 10^{22} \text{ cm}^{-2}$
Cont. norm	cutoffpl(1).norm	$0.331^{+0.028}_{-0.026}$
Γ	cutoffpl(1).PhoIndex	0.733 ± 0.027
E_{CRFS}	gabs(1).LineE	$52.0 \pm 1.3 \text{ keV}$
σ_{CRFS}	gabs(1).Sigma	10 keV*
A_{CRFS}	gabs(1).Strength	27 ± 4
A_{Fe}	egauss(1).area	$(1.3 \pm 0.4) \times 10^{-3} \text{ ph s}^{-1} \text{ cm}^{-2}$
E_{Fe}	egauss(1).center	$6.44 \pm 0.04 \text{ keV}$
$\chi^2/\text{d.o.f} = 435.64/236 = 1.85$		

Parameter name	model component	value
Cov. Frac	constant(100).factor	0.447 ± 0.023
$N_{\text{H},1}$	tbnew_ simple(1).nH	$1.53 \pm 0.08 \times 10^{22} \text{ cm}^{-2}$
$N_{\text{H},2}$	tbnew_ simple(2).nH	$9.7 \pm 0.7 \times 10^{22} \text{ cm}^{-2}$
Cont. norm	cutoffpl(1).norm	0.384 ± 0.009
Γ	cutoffpl(1).PhoIndex	$0.742^{+0.010}_{-0.009}$
E_{CRFS}	gabs(1).LineE	$51.5 \pm 1.0 \text{ keV}$
σ_{CRFS}	gabs(1).Sigma	10 keV^*
A_{CRFS}	gabs(1).Strength	32 ± 4
A_{Fe}	egauss(1).area	$(1.7 \pm 0.4) \times 10^{-3} \text{ ph s}^{-1} \text{ cm}^{-2}$
E_{Fe}	egauss(1).center	$6.428^{+0.026}_{-0.023} \text{ keV}$
$\chi^2/\text{d.o.f} = 413.83/283 = 1.46$		

Parameter name	model component	value
Cov. Frac	constant(100).factor	$0.629^{+0.017}_{-0.016}$
$N_{\text{H},1}$	tbnew_ simple(1).nH	$1.48 \pm 0.05 \times 10^{22} \text{ cm}^{-2}$
$N_{\text{H},2}$	tbnew_ simple(2).nH	$24.5^{+2.7}_{-2.6} \times 10^{22} \text{ cm}^{-2}$
Cont. norm	cutoffpl(1).norm	$0.333^{+0.017}_{-0.016}$
Γ	cutoffpl(1).PhoIndex	$0.647^{+0.018}_{-0.017}$
E_{CRFS}	gabs(1).LineE	$50.5^{+1.2}_{-1.0} \text{ keV}$
σ_{CRFS}	gabs(1).Sigma	10 keV^*
A_{CRFS}	gabs(1).Strength	$23.2^{+2.5}_{-2.2}$
A_{Fe}	egauss(1).area	$(1.6 \pm 0.4) \times 10^{-3} \text{ ph s}^{-1} \text{ cm}^{-2}$
E_{Fe}	egauss(1).center	$6.424^{+0.024}_{-0.020} \text{ keV}$
$\chi^2/\text{d.o.f} = 623.64/286 = 2.18$		

Parameter name	model component	value
Cov. Frac	constant(100).factor	0.64 ± 0.05
$N_{\text{H},1}$	tbnew_ simple(1).nH	$5.7^{+0.5}_{-0.4} \times 10^{22} \text{ cm}^{-2}$
$N_{\text{H},2}$	tbnew_ simple(2).nH	$1.24^{+0.12}_{-0.13} \times 10^{22} \text{ cm}^{-2}$
Cont. norm	cutoffpl(1).norm	0.424 ± 0.008
Γ	cutoffpl(1).PhoIndex	0.851 ± 0.007
E_{CRFS}	gabs(1).LineE	$52.5^{+1.8}_{-3.9} \text{ keV}$
σ_{CRFS}	gabs(1).Sigma	$2.9^{+0.4}_{-2.8} \text{ keV}$
A_{CRFS}	gabs(1).Strength	$5.6^{+3.3}_{-2.9}$
A_{Fe}	egauss(1).area	$(1.9 \pm 0.4) \times 10^{-3} \text{ ph s}^{-1} \text{ cm}^{-2}$
E_{Fe}	egauss(1).center	$6.416^{+0.022}_{-0.019} \text{ keV}$
$\chi^2/\text{d.o.f} = 680.32/290 = 2.35$		

Parameter name	model component	value
Cov. Frac	constant(100).factor	$0.654^{+0.015}_{-0.014}$
$N_{\text{H},1}$	tbnew_ simple(1).nH	$11.3 \pm 0.5 \times 10^{22} \text{ cm}^{-2}$
$N_{\text{H},2}$	tbnew_ simple(2).nH	$1.95^{+0.07}_{-0.08} \times 10^{22} \text{ cm}^{-2}$
Cont. norm	cutoffpl(1).norm	$1.170^{+0.024}_{-0.023}$
Γ	cutoffpl(1).PhoIndex	1.208 ± 0.008
E_{CRFS}	gabs(1).LineE	$40.10^{+19.90}_{-0.11} \text{ keV}$
σ_{CRFS}	gabs(1).Sigma	0 keV*
A_{CRFS}	gabs(1).Strength	0*
A_{Fe}	egauss(1).area	$(2.7^{+0.4}_{-0.5}) \times 10^{-3} \text{ ph s}^{-1} \text{ cm}^{-2}$
E_{Fe}	egauss(1).center	$6.406^{+0.022}_{-0.020} \text{ keV}$
$\chi^2/\text{d.o.f} = 1844.97/364 = 5.07$		

Parameter name	model component	value
Cov. Frac	constant(100).factor	1*
$N_{\text{H},1}$	tbnew_ simple(1).nH	$1.543 \pm 0.020 \times 10^{22} \text{ cm}^{-2}$
$N_{\text{H},2}$	tbnew_ simple(2).nH	$0 \times 10^{22} \text{ cm}^{-2*}$
Cont. norm	cutoffpl(1).norm	0.330 ± 0.004
Γ	cutoffpl(1).PhoIndex	0.728 ± 0.005
E_{CRFS}	gabs(1).LineE	$50.7^{+2.0}_{-1.5} \text{ keV}$
σ_{CRFS}	gabs(1).Sigma	$5.4^{+1.0}_{-0.9} \text{ keV}$
A_{CRFS}	gabs(1).Strength	$9.7^{+2.5}_{-1.9}$
A_{Fe}	egauss(1).area	$(0.8 \pm 0.4) \times 10^{-3} \text{ ph s}^{-1} \text{ cm}^{-2}$
E_{Fe}	egauss(1).center	$6.42^{+0.05}_{-0.04} \text{ keV}$
$\chi^2/\text{d.o.f} = 766.75/306 = 2.51$		

B. Best fit parameters of phase resolved spectra with blackbody model

Table B.1.: Best fit parameters of the global parameters with blackbody model. * denotes frozen value because of limit violation.

Table B.2.: Best fit parameters of phase 0.0–0.125 with blackbody model. * denotes a value that was frozen because of limit violation.

Table B.3.: Best fit parameters of phase 0.125–0.25 with blackbody model. * denotes a value that was frozen because of limit violation.

Table B.4.: Best fit parameters of phase 0.25–0.375 with blackbody model. * denotes value that was frozen because of limit violation.

Table B.5.: Best fit parameters of phase 0.375–0.5 with blackbody model. * denotes value that was frozen because of limit violation.

Table B.6.: Best fit parameters of phase 0.5–0.625 with blackbody model. * denotes value that was frozen because of limit violation.

Table B.7.: Best fit parameters of phase 0.625–0.75 with blackbody model.

Table B.8.: Best fit parameters of phase 0.75–0.875 with blackbody model. * denotes value that was frozen because of limit violation. The cyclotron line energy E_{CRFS} is not valid, as the other parameters of the line are frozen to zero. Errors represent the given limits of the line energy.

Table B.9.: Best fit parameters of phase 0.875–1.0 with blackbody model.

Global parameter name	model component	value
CC XIS0	constant(1).factor	0.9582 ± 0.0020
CC XIS1	constant(2).factor	0.9904 ± 0.0020
CC PIN	constant(4).factor	1.071 ± 0.006
CC GSO	constant(5).factor	0.500*
E_{fold}	cutoffpl(1).HighECut	$12.74 \pm 0.05 \text{ keV}$

Parameter name	model component	value
N_{H}	tbnew_ simple(1).nH	$1.32 \pm 0.05 \times 10^{22} \text{ cm}^{-2}$
Cont. norm	cutoffpl(1).norm	$0.210^{+0.014}_{-0.013}$
Γ	cutoffpl(1).PhoIndex	0.472 ± 0.022
E_{CRFS}	gabs(1).LineE	$53.7^{+2.0}_{-1.9} \text{ keV}$
σ_{CRFS}	gabs(1).Sigma	10 keV*
A_{CRFS}	gabs(1).Strength	18^{+5}_{-4}
A_{Fe}	egauss(1).area	$(2.0 \pm 0.4) \times 10^{-3} \text{ ph s}^{-1} \text{ cm}^{-2}$
E_{Fe}	egauss(1).center	$6.429^{+0.024}_{-0.019} \text{ keV}$
BB. norm	bbody(1).norm	0.0176 ± 0.0014
kT	bbody(1).kT	$1.589^{+0.032}_{-0.029} \text{ keV}$
$\chi^2/\text{d.o.f} = 448.47/341 = 1.32$		

Parameter name	model component	value
N_{H}	tbnew_ simple(1).nH	$1.21 \pm 0.05 \times 10^{22} \text{ cm}^{-2}$
Cont. norm	cutoffpl(1).norm	0.189 ± 0.010
Γ	cutoffpl(1).PhoIndex	$0.466^{+0.019}_{-0.020}$
E_{CRFS}	gabs(1).LineE	$54.2^{+2.6}_{-2.5} \text{ keV}$
σ_{CRFS}	gabs(1).Sigma	10 keV*
A_{CRFS}	gabs(1).Strength	14^{+5}_{-4}
A_{Fe}	egauss(1).area	$(1.5 \pm 0.4) \times 10^{-3} \text{ ph s}^{-1} \text{ cm}^{-2}$
E_{Fe}	egauss(1).center	$6.42^{+0.05}_{-0.04} \text{ keV}$
BB. norm	bbody(1).norm	$0.0130^{+0.0012}_{-0.0010}$
kT	bbody(1).kT	$1.79 \pm 0.06 \text{ keV}$
$\chi^2/\text{d.o.f} = 400.62/307 = 1.30$		

Parameter name	model component	value
N_{H}	tbnew_ simple(1).nH	$1.39^{+0.05}_{-0.04} \times 10^{22} \text{ cm}^{-2}$
Cont. norm	cutoffpl(1).norm	$0.157^{+0.006}_{-0.005}$
Γ	cutoffpl(1).PhoIndex	$0.430^{+0.023}_{-0.018}$
E_{CRFS}	gabs(1).LineE	$55.3^{+2.5}_{-2.2} \text{ keV}$
σ_{CRFS}	gabs(1).Sigma	10 keV*
A_{CRFS}	gabs(1).Strength	23^{+7}_{-5}
A_{Fe}	egauss(1).area	$(1.6 \pm 0.4) \times 10^{-3} \text{ ph s}^{-1} \text{ cm}^{-2}$
E_{Fe}	egauss(1).center	$6.438^{+0.029}_{-0.026} \text{ keV}$
BB. norm	bbody(1).norm	$0.0085^{+0.0034}_{-0.0027}$
kT	bbody(1).kT	$3.5^{+0.4}_{-0.5} \text{ keV}$
$\chi^2/\text{d.o.f} = 412.56/236 = 1.75$		

Parameter name	model component	value
N_{H}	tbnew_ simple(1).nH	$1.38_{-0.06}^{+0.07} \times 10^{22} \text{ cm}^{-2}$
Cont. norm	cutoffpl(1).norm	$0.095_{-0.008}^{+0.009}$
Γ	cutoffpl(1).PhoIndex	$0.193_{-0.030}^{+0.029}$
E_{CRFS}	gabs(1).LineE	$48.5_{-0.8}^{+0.9} \text{ keV}$
σ_{CRFS}	gabs(1).Sigma	10 keV*
A_{CRFS}	gabs(1).Strength	$29.9_{-2.3}^{+2.6}$
A_{Fe}	egauss(1).area	$(1.5 \pm 0.4) \times 10^{-3} \text{ ph s}^{-1} \text{ cm}^{-2}$
E_{Fe}	egauss(1).center	$6.428_{-0.024}^{+0.025} \text{ keV}$
BB. norm	bbody(1).norm	0.0224 ± 0.0014
kT	bbody(1).kT	$1.84 \pm 0.04 \text{ keV}$
$\chi^2/\text{d.o.f} = 617.39/283 = 2.18$		

Parameter name	model component	value
N_{H}	tbnew_ simple(1).nH	$1.16 \pm 0.04 \times 10^{22} \text{ cm}^{-2}$
Cont. norm	cutoffpl(1).norm	0.142 ± 0.005
Γ	cutoffpl(1).PhoIndex	$0.322_{-0.016}^{+0.015}$
E_{CRFS}	gabs(1).LineE	$57.1_{-2.0}^{+2.2} \text{ keV}$
σ_{CRFS}	gabs(1).Sigma	10 keV*
A_{CRFS}	gabs(1).Strength	23_{-5}^{+6}
A_{Fe}	egauss(1).area	$(1.9 \pm 0.4) \times 10^{-3} \text{ ph s}^{-1} \text{ cm}^{-2}$
E_{Fe}	egauss(1).center	$6.420_{-0.019}^{+0.020} \text{ keV}$
BB. norm	bbody(1).norm	0.0223 ± 0.0020
kT	bbody(1).kT	$3.09 \pm 0.13 \text{ keV}$
$\chi^2/\text{d.o.f} = 444.85/286 = 1.56$		

Parameter name	model component	value
N_{H}	tbnew_ simple(1).nH	$1.33 \pm 0.05 \times 10^{22} \text{ cm}^{-2}$
Cont. norm	cutoffpl(1).norm	0.094 ± 0.007
Γ	cutoffpl(1).PhoIndex	0.264 ± 0.023
E_{CRFS}	gabs(1).LineE	$52.2_{-1.9}^{+1.8} \text{ keV}$
σ_{CRFS}	gabs(1).Sigma	$3.3 \pm 1.0 \text{ keV}$
A_{CRFS}	gabs(1).Strength	$8.0_{-2.7}^{+3.6}$
A_{Fe}	egauss(1).area	$(1.9 \pm 0.4) \times 10^{-3} \text{ ph s}^{-1} \text{ cm}^{-2}$
E_{Fe}	egauss(1).center	$6.420_{-0.019}^{+0.018} \text{ keV}$
BB. norm	bbody(1).norm	0.0228 ± 0.0010
kT	bbody(1).kT	$1.523 \pm 0.018 \text{ keV}$
$\chi^2/\text{d.o.f} = 575.95/290 = 1.99$		

Parameter name	model component	value
N_{H}	tbnew_ simple(1).nH	$1.21 \pm 0.05 \times 10^{22} \text{ cm}^{-2}$
Cont. norm	cutoffpl(1).norm	0.086 ± 0.007
Γ	cutoffpl(1).PhoIndex	0.273 ± 0.026
E_{CRFS}	gabs(1).LineE	$41.8_{-1.9}^{+18.2} \text{ keV}$
σ_{CRFS}	gabs(1).Sigma	0 keV^*
A_{CRFS}	gabs(1).Strength	0^*
A_{Fe}	egauss(1).area	$(1.4 \pm 0.4) \times 10^{-3} \text{ ph s}^{-1} \text{ cm}^{-2}$
E_{Fe}	egauss(1).center	$6.405_{-0.029}^{+0.030} \text{ keV}$
BB. norm	bbody(1).norm	0.0516 ± 0.0013
kT	bbody(1).kT	$1.733 \pm 0.012 \text{ keV}$
$\chi^2/\text{d.o.f} = 773.53/364 = 2.13$		

Parameter name	model component	value
N_{H}	tbnew_ simple(1).nH	$1.16 \pm 0.04 \times 10^{22} \text{ cm}^{-2}$
Cont. norm	cutoffpl(1).norm	0.160 ± 0.008
Γ	cutoffpl(1).PhoIndex	0.394 ± 0.017
E_{CRFS}	gabs(1).LineE	$49.9_{-1.8}^{+2.3} \text{ keV}$
σ_{CRFS}	gabs(1).Sigma	$5.1_{-1.0}^{+1.4} \text{ keV}$
A_{CRFS}	gabs(1).Strength	$7.4_{-1.8}^{+2.4}$
A_{Fe}	egauss(1).area	$(1.8 \pm 0.4) \times 10^{-3} \text{ ph s}^{-1} \text{ cm}^{-2}$
E_{Fe}	egauss(1).center	$6.427_{-0.026}^{+0.027} \text{ keV}$
BB. norm	bbody(1).norm	$0.0109_{-0.0008}^{+0.0009}$
kT	bbody(1).kT	$1.057_{-0.027}^{+0.026} \text{ keV}$
$\chi^2/\text{d.o.f} = 470.61/305 = 1.54$		

Acknowledgements

This Bachelor thesis would not have been possible without the help and support of numerous people, whom I want to express my gratitude in this section. First of all, I want to thank my advisor Jörn Wilms, for finding a subject especially suitable for my interests, his help and advises and also for his patience with a beginner's mistakes. I also want to thank Matthias Kühnel for his great introduction to X-ray data analysis and physics of neutron stars and his considerable help to solve software problems. Sebastian Müller helped me with discussions on the source and on continuum models. Felix Fürst already started an analysis of this particular data set and his results have been an important guideline for me. I also want to thank Gabriele Schönherr for helpful discussions on phase lags. Last but not least, I'm also very grateful to my office mates in particular and all other Remeisen in general for making the observatory a really pleasant place to work.

Erklärung

Hiermit erkläre ich, diese Bachelorarbeit in Eigenarbeit angefertigt zu haben, sofern nicht explizit in Text oder Referenzen vermerkt. Diese Arbeit ist der Universität Erlangen-Nürnberg als Voraussetzung für den Erhalt des Abschlusses *Bachelor of Science* vorgelegt worden. Ich erkläre, dass diese Arbeit weder partiell noch als Ganzes für den Erhalt eines anderweitigen Abschlusses verwendet wurde und wird.

Bamberg, den 02.09.2013
Ort, Datum

Ralf Ballhausen